UNIVERSIDADE FEDERAL DE PERNAMBUCO
CENTRO DE CIÊNCIAS EXATAS E DA NATUREZA
DEPARTAMENTO DE FÍSICA
PROGRAMA DE PÓS GRADUAÇÃO EM FÍSICA

CARLOS EDUARDO SANTANA SANTOS

Resonance Structure in Kink-Antikink Interactions

Recife

2024

CARLOS EDUARDO SANTANA SANTOS

Resonance Structure in Kink-Antikink Interactions

Dissertação apresentada ao Programa de Pós Graduação em Física da Universidade Federal de Pernambuco, como requisito parcial para obtenção do título de mestre em física.

Área de Concentração: Física Teórica e Computacional

Orientadora: Azadeh Mohammadi

Recife

2024

.Catalogação de Publicação na Fonte. UFPE - Biblioteca Central

Santos, Carlos Eduardo Santana.
   Resonance Structure in Kink-Antikink Interactions / Carlos Eduardo Santana Santos. - Recife, 2024.
   70f.: il.

   Dissertação (Mestrado) - Universidade Federal de Pernambuco, Centro de Ciências Exatas e da Natureza, Programa de Pós Graduação em Física, 2024.
   Orientação: Azadeh Mohammadi.
   Inclui Referências.

   1. Física de Altas Energias; 2. Estrutura de Ressonância; 3. Defeitos Topológicos. I. Mohammadi, Azadeh. II. Título.

UFPE-Biblioteca Central

CARLOS EDUARDO SANTANA SANTOS

RESONANCE STRUCTURE IN KINK-ANTIKINK INTERACTIONS

Dissertação apresentada ao Programa de Pós-Graduação em Física da Universidade Federal de Pernambuco, como requisito parcial para a obtenção do título de Mestre em Física.

Área de Concentração: Física Teórica e Computacional

Data de aprovação: 22/11/2024.

BANCA EXAMINADORA

_____

Profa. Dra. Azadeh Mohammadi
Orientadora
Universidade Federal de Pernambuco

_____

Prof. Dr. Clécio Clemente de Souza Silva
Examinador Interno
Universidade Federal de Pernambuco

_____

Prof. Dr. Matheus Araújo Marques
Examinador Externo
Universidade Federal da Paraíba

Dedico ao meu pai, Josué Batista de Morais, que não conseguiu ver a conclusão deste trabalho.

ACKNOWLEDGEMENTS

Gostaria de agradecer primeiramente à minha família. Fátima, minha mãe, e Céu, minha madrinha, sem o apoio de vocês, minhas duas mães, nada disso seria possível. Só posso agradecer por acreditarem tanto em mim.

À minha esposa, Júlia, por enxergar luz em mim, mesmo quando eu não via. Por dar suporte à minha vida acadêmica muito antes da graduação em Física. Você tem sido um dos pilares que me dá forças para seguir em frente.

À minha orientadora, Azadeh, e ao amigo e colaborador João Guilherme. Sem vocês, este trabalho não seria possível. Agradeço imensamente por todas as reuniões, conselhos e pela paciência ao longo desses anos, desde a iniciação científica.

Ao Azalab, por toda amizade e acolhimento. Por diversas vezes, nossos encontros e reuniões trouxeram imensa alegria e satisfação aos meus dias. Obrigado por todas as risadas, cafés e discussões calorosas.

Aos meus amigos do departamento e professores, não citarei nomes, pois minha memória não é das melhores e eu não me perdoaria por esquecer alguém. Vocês apoiaram e ajudaram a desenvolver minha vida acadêmica e a tornar o ambiente mais leve e acolhedor.

Por fim, mas não menos importante, aos meus amigos pessoais de toda a vida. Muito obrigado por todo o suporte: Nicholas, Fausto, Bruna, Beatriz, Gabriel e Ítalo.

RESUMO

Defeitos topológicos, que surgem como soluções de teorias de campos, estão intimamente ligados aos fenômenos de transições de fase. Um exemplo fundamental desses defeitos é o kink (e seu contraparte, antikink) em sistemas $(1+1)$ dimensionais, representando soluções estáticas. Quando esses defeitos interagem, exibem uma ampla variedade de comportamentos, incluindo a formação de estruturas fractais. Em modelos bem conhecidos, como a teoria $\lambda\phi^4$, as interações envolvem modos vibracionais localizados, que estão confinados a elementos individuais do sistema. Em contraste, o modelo ϕ^6 apresenta modos deslocalizados que se estendem ao longo do par kink-antikink. Neste último, as frequências dos modos deslocalizados dependem da separação entre o par. Esta dissertação introduz um modelo simplificado baseado em um potencial por partes, $V(\phi) \sim \phi^2$, que facilita a exploração detalhada do fenômeno conhecido como mecanismo de troca de energia. Ajustando dois parâmetros livres, o modelo permite estudar sistematicamente o impacto da adição de frequências localizadas e deslocalizadas e sua interação com a energia cinética dos kinks.

Palavras-chaves: Física de Altas Energias. Kink. Colisão. Estrutura de Ressonância. Modos de Vibração. Defeitos Topológicos.

ABSTRACT

Topological defects, which emerge as solutions to field theories, are intimately linked to phase transition phenomena. A fundamental example of such defects is the kink (and its counterpart, antikink) in $(1+1)$ dimensional systems, representing static solutions. When these defects interact, they exhibit a wide variety of behaviors, including the formation of fractal structures. In well-known models such as the $\lambda\phi^4$ theory, interactions involve localized vibrational modes, which are confined to individual elements of the system. In contrast, the ϕ^6 model features delocalized modes extending across the kink-antikink pair. In the latter, the frequencies of the delocalized modes depend on the pair's separation. This thesis introduces a toy model based on a piecewise potential, $V(\phi) \sim \phi^2$, which facilitates a detailed exploration of the phenomenon known as the energy exchange mechanism. By adjusting two free parameters, the model allows for systematically studying the impact of adding localized and delocalized frequencies and their interplay with the kinetic energy of the kinks.

Keywords: High Energy Physics. Kink. Collision. Resonance Structure. Vibrational Modes. Topological Defects.

LIST OF FIGURES

CONTENTS

1 (1+1)-DIMENSIONAL TOPOLOGICAL DEFECTS

1.1 INTRODUCTION

The classical field theory allows us to describe systems with many degrees of freedom. Instead of a discrete set of free variables that the dynamics depends on, there is a continuum of values.

Our object of study is the scalar field ϕ, which has a spacetime dependence. The dynamics of the field are obtained by minimizing the functional $S[\phi]$, the action in $(1+1)$ dimensions 1.1:

$$S[\phi] = \int_{-\infty}^{\infty} \underbrace{\left(\frac{1}{2}\partial_\mu\phi\partial^\mu\phi - V(\phi)\right)}_{\mathcal{L}} dx\, dt, \tag{1.1}$$

where the function $V(\phi)$ is the potential energy function and $\mathcal{L}$ is the Lagrangian.

Due to the translational symmetry of space and time in the theory, conserved quantities such as energy and momentum densities arise through the conserved energy-momentum tensor:

$$\Theta_{\mu\nu} = \partial_\mu\phi\partial_\nu\phi - \eta_{\mu\nu}\mathcal{L}, \tag{1.2}$$

where $\eta_{\mu\nu}$ = diag(1,-1) is the metric. The energy and momentum densities can be derived from it

$$\begin{cases} \mathcal{P} = -\partial_x\phi\partial_t\phi, \\ \mathcal{H} = \dfrac{1}{2}(\partial_t\phi)^2 + \dfrac{1}{2}(\partial_x\phi)^2 + V(\phi). \end{cases} \tag{1.3}$$

In particular, the action 1.1 can be used to handle wave-equation-like problems. If the potential energy is identically zero, the Euler-Lagrange equations of motion for fields yield the classical wave equation:

$$\frac{\partial^2 y(x,t)}{\partial t^2} - v^2\frac{\partial^2 y(x,t)}{\partial x^2} = 0, \tag{1.4}$$

which allows solutions that obey the superposition principle. However, if $V(\phi) \neq 0$, a class of solutions called solitons and solitary waves can emerge in the model.

Solitons are solutions of the equations of motion that exhibit integrability. While there is no exact definition of integrability, one of the requirements is that the system must have infinitely many conserved quantities. Solitary waves, on the other hand, differ significantly. They can

appear in field theories with similar actions 1.1, but they do not correspond to integrable systems. Nevertheless, it is common in the literature to use the term "soliton" in the context of solitary waves. For clarity, we will refer to the objects studied here as solitons, but it is important to keep this distinction in mind.

Since the action 1.1 has symmetries, a Lorentz boost can be applied, leading to a Lorentz-invariant relation by integrating the densities 1.3:

$$E^2 - P^2 = M^2, \tag{1.5}$$

where E is the energy, P the momentum, and M the mass.

1.2 ENERGY STUDY AND BOGOMOLNY METHOD

Since we know the energy density 1.3, the total energy of the system can be written through an integration process.

$$\begin{aligned}
\mathcal{E} &= \int_{-\infty}^{\infty} \left[\frac{1}{2}(\partial_t\phi)^2 + \frac{1}{2}(\partial_x\phi)^2 + V(\phi)\right] dx, \\
&= \int_{-\infty}^{\infty} \left[\frac{1}{2}(\partial_t\phi)^2 + \frac{1}{2}\left(\partial_x\phi \mp \sqrt{2V(\phi)}\right)^2\right] dx \pm \int_{\phi(-\infty)}^{\phi(+\infty)} \sqrt{2V(\phi')}\, d\phi', \\
&= \int_{-\infty}^{\infty} \left[\frac{1}{2}(\partial_t\phi)^2 + \frac{1}{2}\left(\partial_x\phi \mp \sqrt{2V(\phi)}\right)^2\right] dx \pm \mathcal{E}_{\text{min}},
\end{aligned} \tag{1.6}$$

The latter equation defines the minimum energy of the system and can be rewritten as:

$$\begin{aligned}
\mathcal{E}_{\text{min}} &= \int_{\phi(-\infty)}^{\phi(+\infty)} \sqrt{2V(\phi')} d\phi', \\
&= \int_{\phi(-\infty)}^{\phi(+\infty)} \frac{dW}{d\phi'} d\phi', \\
&= W(\phi(+\infty)) - W(\phi(-\infty)),
\end{aligned} \tag{1.7}$$

defining the prepotential W. This observation is due to Bogomol'nyi (BOGOMOL'NYI, 1976), and energy bounds of this general type, where the energy is bounded from below in terms of solely topological data, are known as Bogomol'nyi bounds.

Replacing the prepotential in 1.9, we reach the so-called Bogomol'nyi-Prasad-Sommerfield (BPS) condition:

$$\partial_x\phi = \pm\frac{dW}{d\phi}. \tag{1.8}$$

This means that we have a first-order differential equation as the equation of motion that also minimizes energy:

$$\begin{cases} \partial_t \phi = 0, \\ \partial_x \phi \mp \sqrt{2V(\phi)} = 0, \end{cases} \tag{1.9}$$

So we can find a solution that minimizes the energy. First of all, the solution must be static since the time derivative is zero. Furthermore, there is an easy way to obtain the solution analytically by using the second equation of 1.9. The boundary conditions help us with this. The field must be finite as the positions go to infinity, and the value of x_0 appears due to the translational symmetry of the system, leading to:

$$x - x_0 = \pm \int_{\phi(-\infty)}^{\phi(+\infty)} \frac{d\phi'}{\sqrt{2V(\phi')}}. \tag{1.10}$$

1.3 TOPOLOGICAL CHARGE

Topologically, the model also has conserved quantities. The current $j^\mu = \dfrac{1}{2\phi(+\infty)} \epsilon^{\mu\nu} \partial_\nu \phi$, where $\mu, \nu = 0, 1$ and $\epsilon^{\mu\nu}$ is the antisymmetric symbol in two dimensions. The conserved charge is:

$$Q = \int_{-\infty}^{\infty} j^0 \, dx = \frac{1}{2\phi(+\infty)} [\phi(+\infty) - \phi(-\infty)], \tag{1.11}$$

For the models we are going to study, the topological charge Q assumes the values ± 1. The solution with $Q = 1$ corresponds to the plus sign in 1.10 and is called a kink. The solution with the minus sign is called an antikink.

1.4 DERRICK'S ARGUMENT

The static solution to 1.9 is crucial for achieving a configuration where the energy is minimized. Starting with a general Lagrangian involving multiple fields, we will verify the conditions to obtain static solutions. Given a field theory and its action as a function of arbitrary scalar fields ϕ^a:

$$S[\phi^a] = \int \left[\frac{1}{2} \sum_a (\partial_\mu \phi^a)^2 - V(\phi^a) \right] d^{n+1}x, \tag{1.12}$$

where, as mentioned earlier, $V(\phi^a) \geq 0$. For static solutions, the field configurations satisfy $\phi^a \to \phi_0^a$, and time derivatives in 1.12 vanish:

$$S[\phi_0^a] = \int \left[\frac{1}{2} \sum_a (\nabla \phi_0^a)^2 - V(\phi^a) \right] d^{n+1}x, \tag{1.13}$$

resulting in the energy of the field configuration as:

$$\mathcal{E}[\phi_0^a] = \int \left[\frac{1}{2} (\nabla \phi_0^a)^2 + V(\phi_0^a) \right] d^{n+1}x. \tag{1.14}$$

We now transform our coordinate system by rescaling $x^j \to \alpha x^j$ (modifying only the spatial coordinates), with $\alpha > 0$, and introduce new variables $y^j = \alpha x^j$. The energy as a function of the new field configuration $\psi_0^a(y)$ becomes:

$$\mathcal{E}[\psi_0^a] = \int \left[\frac{\alpha^{2-n}}{2} (\nabla \psi_0^a(y))^2 + \alpha^{-n} V(\psi_0^a(y)) \right] d^{n+1}y. \tag{1.15}$$

Since the first term in 1.15 is always positive, it follows that:

$$\mathcal{E}[\psi_0^a] < \mathcal{E}[\phi_0^a], \tag{1.16}$$

for $n \geq 2$, implying that the energy is not minimized when $\alpha \to 1$. Therefore, static and stable field configurations do not minimize the energy in dimensions higher than one. These configurations are only possible if $n = 1$.

2 POTENTIALS

In the previous chapter, we saw that the potential of our field theory must obey a few properties since we are searching for stable, particle-like solutions that continuously connect two vacua of the potential. Now, we will see a few examples of the models with the solutions with these properties. We have the freedom to choose the potential $V(\phi)$, it should be a non-negative function of the field.

2.1 THE $\lambda\phi^4$ MODEL

2.1.1 Motivation

Starting with the $\lambda\phi^4$ model is not random. In fact, this model appears in several areas of physics. First of all, Landau (GINZBURG; LANDAU, 1965) used it to describe second-order phase transition phenomena, demonstrating in a phenomenological way the theory of superconductors. Although we are presenting the historical context of the $\lambda\phi^4$ model, the field theory of superconductors is quite different from the scalar field discussed here, as it involves a complex scalar field and a vector field.

In the particle physics context, the $\lambda\phi^4$ model is used in the Higgs Mechanism to explain how the fundamental particles of physics obtain mass (HIGGS, 1964). In the realm of quantum field theory, this model is often used as a toy model for interacting field theories, as extensively discussed in (PESKIN; SCHROEDER, 2019) and (TONG, 2006). Finally, when we couple a fermion field with the bosonic one from $\lambda\phi^4$, we obtain a toy model for nuclear physics (CAMPBELL; LIAO, 1976) and study the effect of the bosonic field and its topology on the fermion number (JACKIW; REBBI, 1976).

The solutions we will find in the next chapter for some potentials are called Topological Defects. They are the most straightforward solutions because we will only deal with $(1+1)D$ field theories. As the area of topological defects is very rich in literature, We recommend checking more details in consecrated textbooks like (RAJARAMAN, 1982), (VACHASPATI, 2006), and (MANTON; SUTCLIFFE, 2010).

In the next section, we will do a process that can be applied to any potential $V(\phi)$ that obeys the conditions we have discussed from the beginning. Once the process is understood, we can apply it to any potential other than $\lambda\phi^4$.

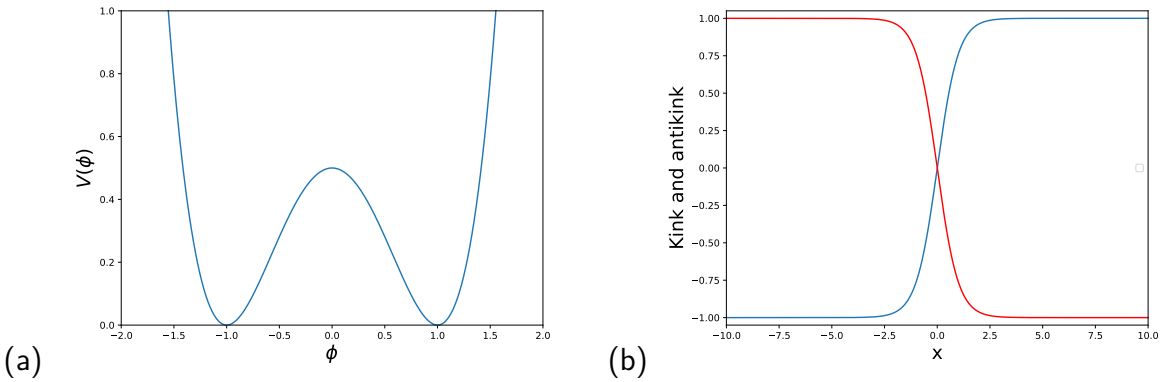

(a) (b)

Figure 1 – (a) The $\lambda\phi^4$ potential and (b) the pair kink (blue) and antikink (red). The values are $\lambda = 2$ and $m = 1$. Source: The Author (2024).

2.1.2 The potential

Let us now study the potential $\frac{\lambda}{4}(\phi^2 - m^2)^2$ shown in Fig. 1 It is interesting to notice that the potential shown in Fig. 1.a) has the properties discussed in chapter 1. The Lagrangian of the problem is given by

$$\mathcal{L} = \frac{1}{2}\partial_\mu\phi\partial^\mu\phi - \frac{\lambda}{4}(\phi^2 - m^2)^2, \tag{2.1}$$

and consequently the equation of motion are given in 2.1

$$\partial_t^2\phi - \partial_x\phi + \lambda(\phi^2 - m^2)\phi = 0. \tag{2.2}$$

We need to search for static solutions that obey

$$x - x_o = \pm\int_{-m}^{+m} \frac{d\phi}{\sqrt{\frac{\lambda}{2}(\phi^2 - m^2)^2}}, \tag{2.3}$$

which can be easily integrated to obtain two different solutions

$$\begin{cases} \phi_{\mathrm{K}} = m\tanh\left(\sqrt{\frac{\lambda}{2}}m(x - x_o)\right), \\ \phi_{\bar{\mathrm{K}}} = -m\tanh\left(\sqrt{\frac{\lambda}{2}}m(x - x_o)\right). \end{cases} \tag{2.4}$$

The solutions 2.4 are, respectively, the kink and antikink of the model and can be seen in Fig. 1.b). The kink solution is a static solution of the equations of motion that connects the vacua $-m$ to $+m$ of the potential shown in 1. The antikink is similar but connects the vacua in the opposite direction.

Once we have found the static solution, it is possible to obtain the time-dependent solution by applying a Lorentz boost to these solutions. If the velocity of the kink is v, then we set $X = \gamma(x - x_0 + vt)$ to reach the traveling solutions:

$$\phi_{\mathsf{K}}(x,t) = m \tanh\left(\sqrt{\frac{\lambda}{2}} mX\right). \tag{2.5}$$

2.1.3 Conserved Quantities

As we mentioned in Chapter 1, there are particle-like solutions that arise from non-linear wave equations. This becomes clear if we study the energy of these solutions. By using the methods we studied before, we can obtain the static energy density $\mathcal{H}$ using the functions 2.4:

$$\begin{aligned} \mathcal{H} &= \frac{1}{2}\left(\frac{d\phi_{\mathsf{K}}}{dx}\right)^2 + \frac{\lambda}{4}(\phi_{\mathsf{K}}^2 - m^2)^2, \\ &= \frac{\lambda m^4}{2}\mathsf{sech}^4\left(\sqrt{\frac{\lambda}{2}} mx\right). \end{aligned} \tag{2.6}$$

The energy density concentrates around the center of the kink profile as shown in Fig. 2.

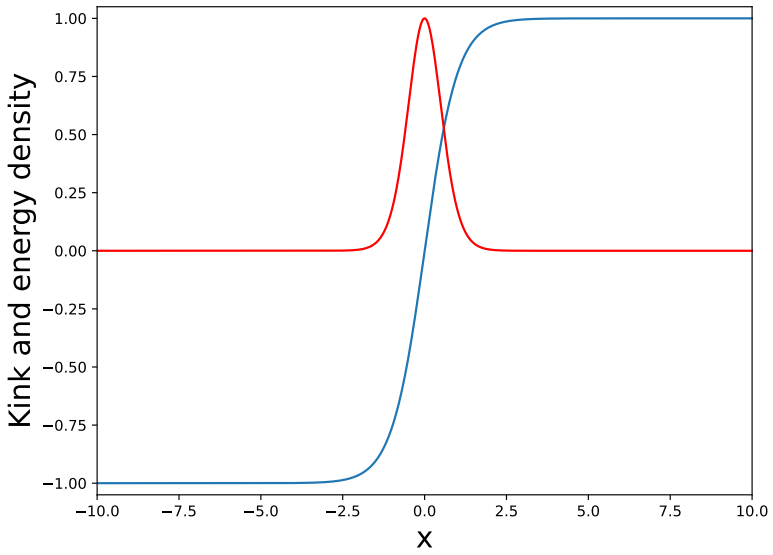

Figure 2 – $\lambda\phi^4$ energy density (red) and kink solution (blue). The values are $m = 1$ and $\lambda = 2$. Source: The Author (2024).

Since the Lagrangian has translational symmetry, it means that there is no cost to move this energy density from one place to another. Consequently, a zero mode, also called a translational

mode, must exist. It can be found by investigating fluctuations in the kink solution

$$\phi(x,t) = \phi_{\mathsf{K}}(x) + \eta(x)\cos(\omega t). \tag{2.7}$$

By substituting 2.7 into the equation of motion 2.2, we obtain a Schrödinger-like equation

$$-\partial_x^2\eta(x) + [4 - 7\mathsf{sech}^2(x)]\eta(x) = \omega^2\eta(x) \tag{2.8}$$

. The potential in 2.8, $U(x) = 4 - 7\mathsf{sech}^2(x)$ shown in Fig. 3, is a Pöschl-Teller type one resulting in analytical modes and spectrum for the above differential equation.

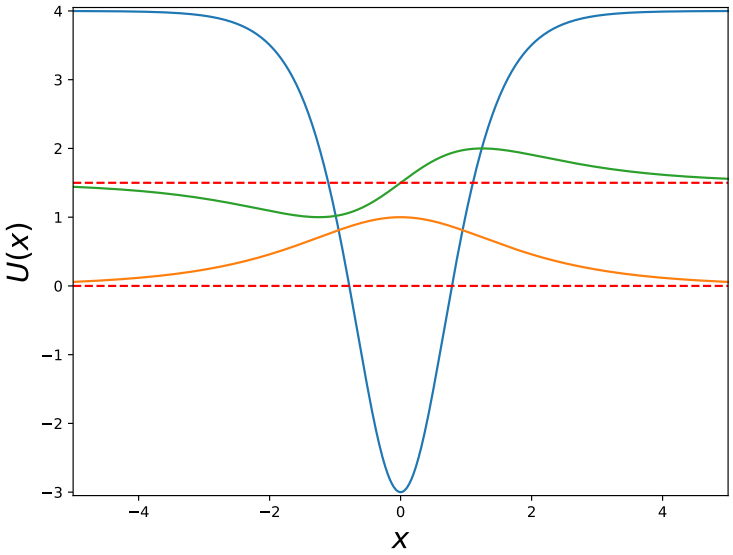

Figure 3 – The linearized potential $U(x)$ for the $\lambda\phi^4$ model is shown in the figure. The red dotted lines represent the eigenvalues $\omega_0^2 = 0$ and $\omega_1^2 = 3/2$. The blue solid line represents the potential $U(x)$, the orange solid line is the first eigenfunction η_0, and the green solid line is the second eigenfunction η_1. Source: The Author (2024).

There are two discrete solutions given by $\omega_0^2 = 0$ and $\omega_1^2 = 3/2$ (SUGIYAMA, 1979). The first one is the frequency of the zero mode arising from the translational symmetry of the system. The second one is the massive vibrational mode bound to the kink. The latter one gives origin to a resonance phenomenon that will be explored in the next chapter. For $\omega^2 > 2$, there are infinitely many solutions, forming a continuous spectrum. This continuum corresponds physically to radiation that propagates to spatial infinity. The modes associated

to the above normal modes are as follows

$$\begin{cases} \omega_0^2 = 0 \longrightarrow \eta_0(x) = \sqrt{\dfrac{3}{4\sqrt{2}}}\mathrm{sech}^2\left(\dfrac{x}{\sqrt{2}}\right), \\ \omega_1^2 = \dfrac{3}{2} \longrightarrow \eta_1(x) = \sqrt{\dfrac{3}{2\sqrt{2}}}\tanh\left(\dfrac{x}{\sqrt{2}}\right)\mathrm{sech}\left(\dfrac{x}{\sqrt{2}}\right), \\ \omega_n^2 = n^2+2 \longrightarrow \eta_n(x) = N_n e^{inx}\left[3\tanh^2\left(\dfrac{x}{\sqrt{2}}\right) - 1 - 2n^2 - 3\sqrt{2}in\tanh\left(\dfrac{x}{\sqrt{2}}\right)\right], \end{cases} \tag{2.9}$$

where N_n is given by $N_n^{-2} = 4\pi\left[2(n^2+1)^2 + n^2\right]$. The discrete solutions and the potential can be seen in Fig. 3.

2.1.4 Rescaling

Since we plan to solve some differential equations numerically, we need to rescale the physical parameters to work with dimensionless ones. It is convenient to change variables in the following form

$$\begin{cases} \phi \longrightarrow \dfrac{\phi}{m}, \\ x^\mu \longrightarrow \sqrt{\lambda} m x^\mu. \end{cases} \tag{2.10}$$

The Lagrangian with the dimensionless parameters become

$$\mathcal{L} = \frac{1}{2}\partial_\mu\phi\partial^\mu\phi - \frac{1}{4}(\phi^2-1)^2. \tag{2.11}$$

Integrating the energy density in the whole space leads to $E_{\phi^4} = \dfrac{\sqrt{2}}{3}$ for the kink (antikink) of the model.

2.1.5 Interactions

The kink and antikink pair interact via the static force between them. The purpose of this section is to understand how this interaction works. Since they are particle-like objects, the first thing that comes to mind is their behavior during collisions. We position the kink at $x = -x_0$ and the antikink at $x = +x_0$. But why are we considering two different types of topological defects (kink and antikink) instead of two kinks or two antikinks?

The reason is that during the collision, the kink-antikink ($\mathrm{K\bar{K}}$) and antikink-kink ($\mathrm{\bar{K}K}$) pairs exhibit an attractive interaction, while two identical topological defects (either two kinks or two antikinks) show a repulsive interaction. This means that the interaction between two

different types of topological defects is more interesting and complex than the interaction between two identical ones.

We are going to deal with $\phi_{\mathrm{K}}(x+x_0)$ and $\phi_{\bar{\mathrm{K}}}(x-x_0)$. The field configuration is shown in Fig. 4. Furthermore, the initial kink-antikink and antikink-kink conditions to solve the equations of motion are given in 2.12.

$$\begin{cases} \phi_{\mathrm{K}\bar{\mathrm{K}}}(x,0) = \phi_{\mathrm{K}}[\gamma(x+x_o)] + \phi_{\bar{\mathrm{K}}}[\gamma(x-x_o)] - 1, \\ \phi_{\bar{\mathrm{K}}\mathrm{K}}(x,0) = \phi_{\mathrm{K}}[\gamma(x-x_o)] + \phi_{\bar{\mathrm{K}}}[\gamma(x+x_o)]. \end{cases} \tag{2.12}$$

The -1 factor in the first equation of 2.12 serves to ensure that the initial condition remains between the vacuum values ± 1. The ansartz above is valid when we lead with a well separated pair of topological defects.

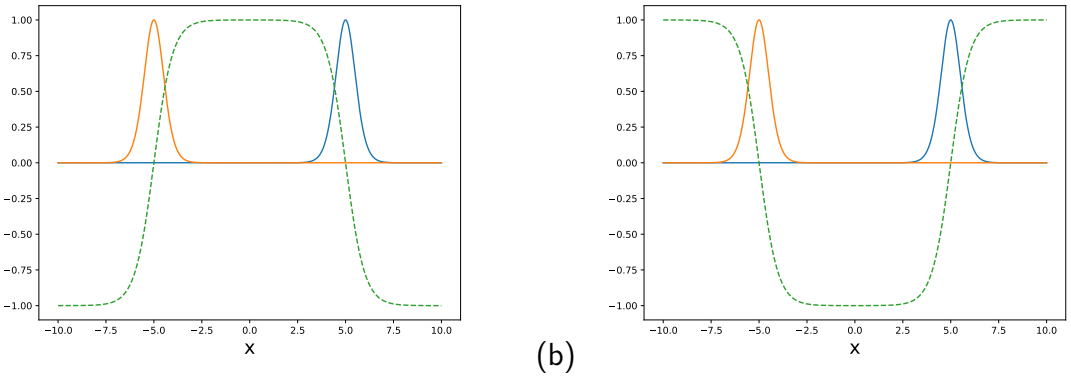

(a) (b)

Figure 4 – (a) The kink-antikink profile (b) the antikink-kink profile. In orange and blue, the energy densities and the dotted lines are the field profiles. Source: The Author (2024).

There is a method to determine the force between the kink-antikink (antikink-kink) pair. We need to use the momentum P can be obtained by integrating the momentum density 1.3

$$P = -\int_{\text{kink}} \partial_t\phi\partial_x\phi\, dx. \tag{2.13}$$

We can use the scheme described in Fig. 5 to avoid infinities. So, our integration process in equation 2.13 becomes

$$P = -\int_{-x_o-D}^{-x_o+D} \partial_t\phi\partial_x\phi\, dx. \tag{2.14}$$

The force can be calculated by differentiating the equation with respect to time. We can use the initial field configuration given by the first equation in 2.12 and assume that the pair is initially at rest

$$F = \Big[-\partial_x\phi_{\mathrm{K}}\partial_x\phi_{\bar{K}} + V(\phi(x,0)) - V(\phi_{\bar{K}}) - V(\phi_K) \Big]_{-x_o-D}^{-x_o+D}. \tag{2.15}$$

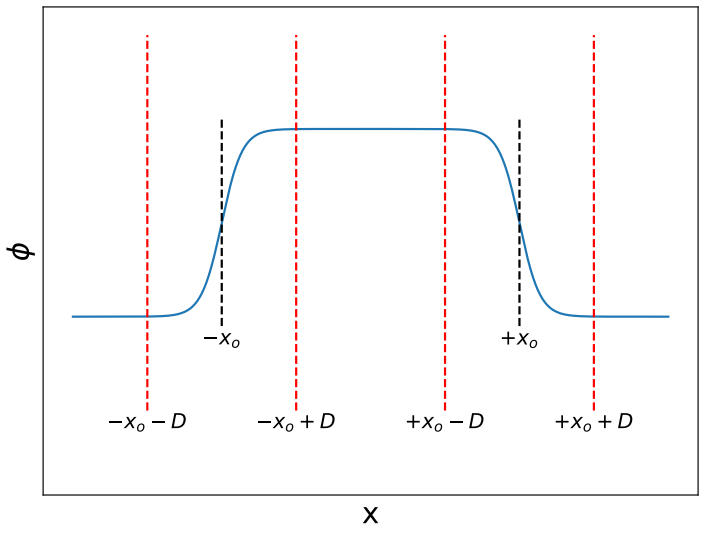

Figure 5 – Scheme to calculate the force between the kink-antikink pair. To avoid infinities, we need to make the integral between $-x_o - D$ and $+x_o + D$, since in the left (right) part of that interval, the derivatives of the field quickly decay to zero. Source: The Author (2024).

Finally, by using the second-order Taylor series expansion for the potential terms and applying the kink-antikink solutions 2.4, we obtain

$$F \approx \frac{16\lambda^2 m^2}{\lambda} e^{-2\sqrt{2\lambda m^2}x_o}. \tag{2.16}$$

The result obtained in the equation 2.16 shows that the force between the pair is attractive. There is an explanation for why a field configuration with more than one topological defect cannot be static. In the initial configuration, the isolated solutions are static, but they immediately start to attract, leading to acceleration.

2.2 THE "PERFECT" BROTHER: THE SINE-GORDON MODEL

The model we saw in section 2.1 is an example of a non-integrable theory. An example of an integrable theory arises with the sine-Gordon potential $V(\phi) = 1 - \cos\phi$. The potential is shown in Fig. 6. Once we have already seen the calculation of static and energy density configurations, we can proceed faster.

The potential has infinitely many minima since the condition $\phi = 2\pi n$ $(n = 0, \pm 1, \pm 2, \pm 3, \ldots)$ yields zero. This implies that the problem now involves infinitely many topological sectors. Con-

sequently, there is a kink-antikink pair between each pair of subsequent vacuum states, as we can see in Fig. 6.

By using 1.10, the kink-antikink solutions are given by

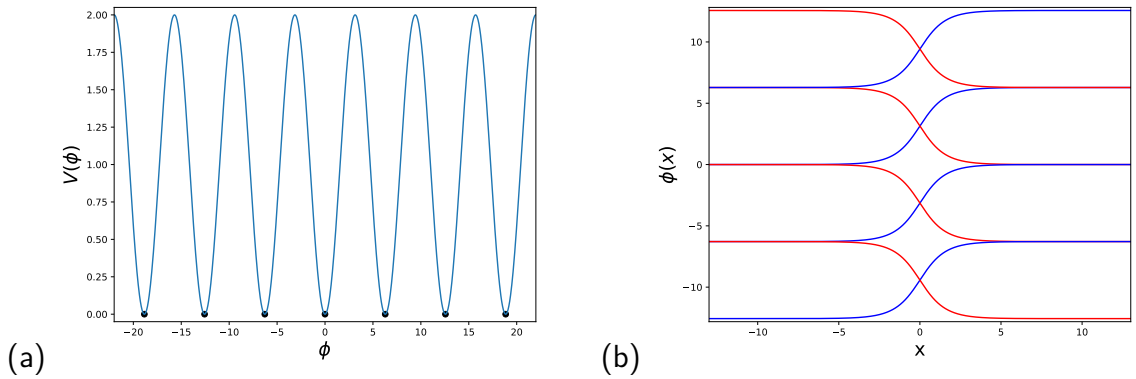

(a) (b)

Figure 6 – (a) The sine-Gordon potential. The dots represent the zeros of the potential. (b) The kink-antikink pairs from different sectors. Source: The Author (2024).

$$\begin{cases} \phi_{\mathsf{K}}(x) = 4\tan^{-1}\left[e^{(x-x_o)}\right] \\ \phi_{\bar{\mathsf{K}}}(x) = 4\tan^{-1}\left[e^{-(x-x_o)}\right]. \end{cases} \tag{2.17}$$

Furthermore, it is also possible to calculate the energy density, which has the same profile as Fig. 2 and is given by $\mathcal{H}(x) = 4\text{sech}^2(x - x_o)$. Integrating it leads to the total energy equal to $E_{\mathsf{sG}} = 8$.

The sine-Gordon model also has a linearized potential, given by $U(x) = \cos[4\arctan(e^x)]$, but the only eigenvalue is $\omega_0^2 = 0$.

2.2.1 Bound States

The sine-Gordon theory allows a type of solution to the equation of motion that is not present in the $\lambda\phi^4$ model. This type of solution, known as breathers, is present in integrable field theories and arises when we put a kink and an antikink together, interacting in a bound state. Such configurations can be seen in Fig. 7.

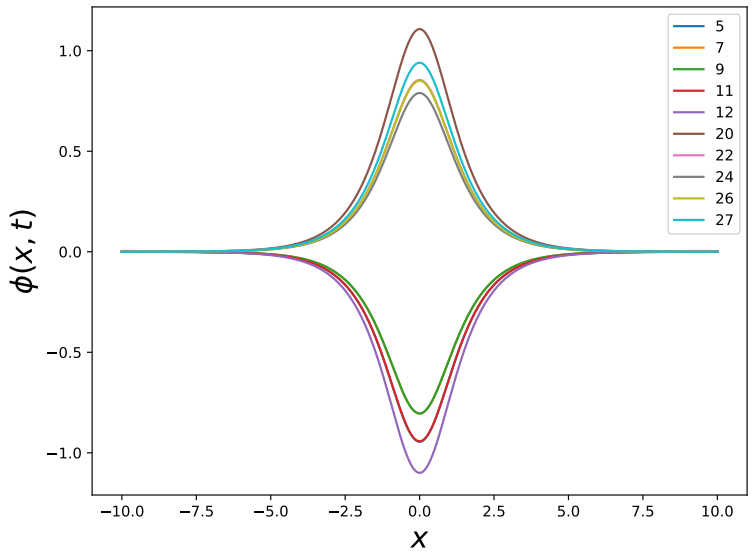

Figure 7 – Breathers field configuration for different times. The parameter v is 0.2. Source: The Author (2024).

The beauty of the bound states in Fig. 7 is that they can be found analytically. There are other bound states in non-integrable theories (such as $\lambda\phi^4$), but we will see them in the next chapter. The breather solutions are

$$\phi_v(x,t) = 4\tan^{-1}\left[\frac{\sin\left(\frac{vt}{\sqrt{1+v^2}}\right)}{v\cosh\left(\frac{x}{\sqrt{1+v^2}}\right)}\right]. \tag{2.18}$$

where v is a free parameter. Despite the fact that this solution is long-lived, it is important to note that the kink-antikink (antikink-kink) configuration also has a force $\sim e^{-2D}$, as we saw in 2.1.5.

The solution given by 2.18 is a bound state of a kink-antikink pair. Although it is a bound state, it is long-lived. This occurs because the theory is what we call integrable, allowing the waves to interact with each other without losing their shape (or energy). It is also possible to have a similar bound state in the case of the $\lambda\phi^4$ potential, but since the theory is non-integrable, the bound state of the kink-antikink quickly decays into radiation. This state is called bion, and we will explore it further in the next chapter.

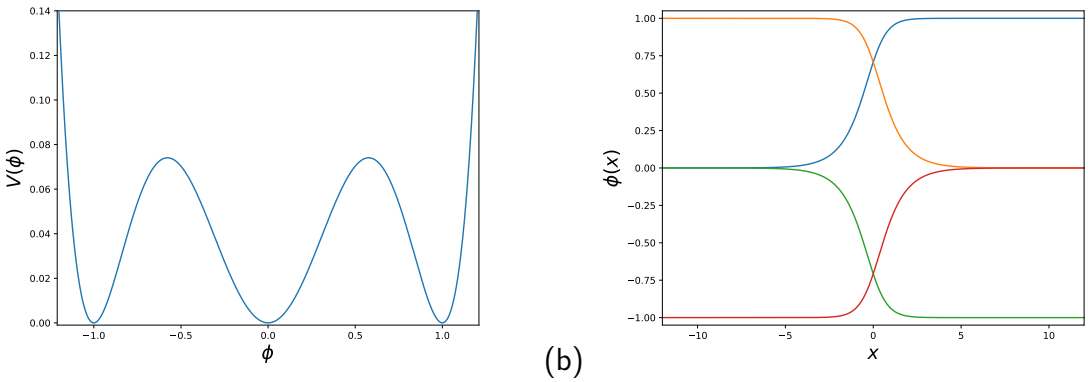

(a) (b)

Figure 8 – (a) The ϕ^6 potential and (b) the pair kink and antikink from both sectors. Source: The Author (2024).

2.3 THE ϕ^6 MODEL

In 2.1, we saw a non-integrable field theory that has only two vacuum states. In 2.2, we saw an integrable field theory that has infinite vacuum states. Now, we are going to add more vacuum states to the well-known $\lambda\phi^4$ model. The second simplest non-integrable field theory is the ϕ^6 model, which has three vacua in the vacuum manifold.

The ϕ^6 potential $V(\phi) = \frac{1}{2}\phi^2(\phi^2-1)^2$ has three vacua, at $\phi = 0, \pm 1$. As a result, we have two different topological sectors and two distinct pairs of kinks and antikinks. The potential and the pair of topological sectors are shown in 9.

Once again, we reach two kink-antikink configurations by using 1.10 with the ϕ^6 potential given above. If we call $\phi_{(0,1)}(x)$ a kink solution from $\phi = 0$ to $\phi = 1$ and also $\phi_{(1,0)}$, the antikink, from 1 to 0, we can use symmetry to write

$$\begin{cases} \phi_{\mathsf{K}}(x) = \phi_{(0,1)}(x) = \sqrt{\dfrac{1+\tanh(x)}{2}}, \\ \phi_{(1,0)} = \phi_{\mathsf{K}}(-x), \\ \phi_{(0,-1)} = -\phi_{\mathsf{K}}(x), \\ \phi_{(-1,0)} = -\phi_{\mathsf{K}}(-x). \end{cases} \tag{2.19}$$

Due to the symmetry of the potential, all these configurations have the same energy, which can be found using the localized energy density $\mathcal{H}(x) = \frac{1}{8}\left[\tanh^3(x) - \tanh^2(x) - \tanh(x) + 1\right]$. All topological defects' mass (energy) in this model equals $M = 1/4$.

The ϕ^6 model is also a non-integrable theory, which means that the solutions cannot form a bound state as found in the sine-Gordon model. Additionally, with one more topological

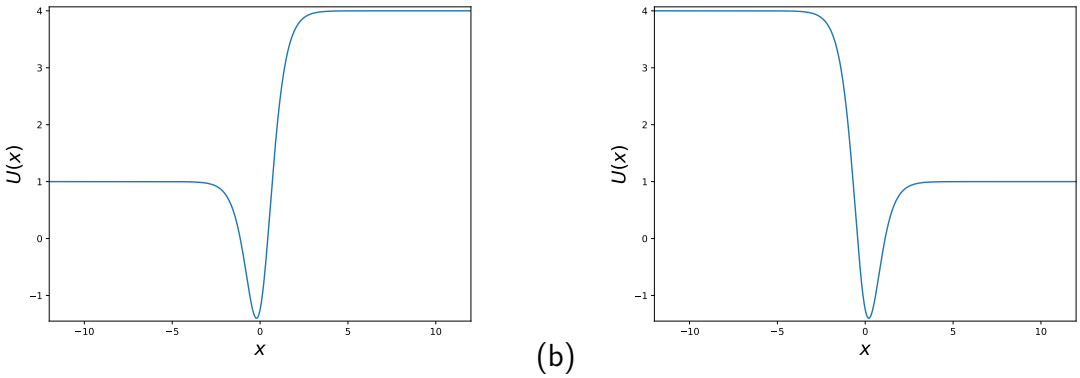

(a) (b)

Figure 9 – Linearized potential for ϕ^6 model. (a) for the kink and (b) for the antikink. Source: The Author (2024).

sector than in the $\lambda\phi^4$ model, the dynamics of the interactions between a kink and an antikink in the ϕ^6 model are quite different. The ϕ^6 model linearized potential is asymmetric in the following form

$$\begin{cases} U_{\mathrm{K}} = 15\phi_{\mathrm{K}}^4 - 12\phi_{\mathrm{K}}^2 + 1, \\ U_{\bar{\mathrm{K}}} = 15\phi_{\bar{\mathrm{K}}}^4 - 12\phi_{\bar{\mathrm{K}}}^2 + 1. \end{cases} \tag{2.20}$$

The potential 2.20 also has only one discrete solution: $\omega_0^2 = 0$, similar to the sine-Gordon model, but there are also continuum solutions which are explored in (LOHE, 1979). The asymmetry shown in Fig. 9 and in equation 2.20 causes the dynamics of the interaction between kink-antikink and antikink-kink to differ in several aspects. These aspects will be explored in the next chapter.

3 INTERACTIONS

Interactions between topological defects have been extensively studied over the last few decades. We will begin with exploring the well-known $\lambda\phi^4$ model.

In 1983, a paper was published by Campbell (CAMPBELL; SCHONFELD; WINGATE, 1983) and his collaborators. Through an extensive numerical approach, they showed that there are three possible outcomes for an interaction between a kink-antikink pair in a non-integrable theory: bion formation, reflection, and resonance. The resonance phenomenon is an intermediate case between bion formation and reflection. In bion formation, the pair undergoes a large number of bounces (collisions) before eventually disappearing, while in reflection, there is only one bounce before they separate and move to infinity. In resonance, there are a finite number of bounces before the pair separates and moves to infinity.

Since then, many other works and new models, inspired by sine-Gordon and $\lambda\phi^4$ ones, have been investigated to explore different aspects of the dynamics. In literature, it is possible to explore modifications of sine-Gordon models in order to get non-integrable models (CAMPBELL; PEYRARD; SODANO, 1986; GANI; KUDRYAVTSEV, 1999; BELENDRYASOVA et al., 2019; GANI; MARJANEH; SAADATMAND, 2019; PAVA; PLAZA, 2021; DOREY et al., 2021a; CARRETERO-GONZáLEZ et al., 2022; MUKHOPADHYAY et al., 2022).

Working on polynomial models, such as $\lambda\phi^4$ and ϕ^6, as discussed in (ROMANCZUKIEWICZ, 2003; HOSEINMARDY; RIAZI, 2010; BELENDRYASOVA; GANI, 2017; DOREY et al., 2017; GANI; MARJANEH; JAVIDAN, 2021; ADAM et al., 2022), has revealed additional phenomena in the literature over the years. When studying the resonance frequency spectra, there is a fine line in the curve of frequencies as a function of the distance between the centers of the kink and antikink. This line is called the spectral wall. The spectral wall phenomenon was discovered in 2019 through (ADAM et al., 2019). Since then, a few other works have explored the phenomenon (ADAM et al., 2022; CAMPOS et al., 2023).

In this chapter, we will explore the interactions between kink-antikink and antikink-kink pairs generated by different potentials. We will begin with the non-integrable $\lambda\phi^4$ model and examine the three different phenomena mentioned above. Next, we will discuss the integrable sine-Gordon model, highlighting the differences arising from integrability. Finally, we will study the ϕ^6 model, focusing on the differences in phenomenology between the dynamics of the $\lambda\phi^4$ and ϕ^6 models.

The integration process going to be done using the methods of the appendix 5.

3.1 $\lambda\phi^4$ POTENTIAL

In 2.1, we already discussed many aspects of the $\lambda\phi^4$ model. The potential and the kink are shown in 1, while the analytic form of the kink-antikink pair is given in 2.4. We will integrate the equation of motion 2.2 using the initial additive ansatz presented in 2.12. Due to the symmetry of the potential 1 and the equality of the linearized potential 3, the kink-antikink and antikink-kink cases yield the same results. Therefore, we will only present the kink-antikink case. Fig. 10 shows the possible results of the collisions for the initial position $x_o = 10$. The large blue regions represent one of the vacua, $\phi(x,t) = -1$. The dark red regions represent the other vacuum, $\phi(x,t) = 1$. The center of the kink-antikink pair is the yellow line, $\phi(x,t) = 0$, which separates the two vacua of the potential.

Fig. 10(a) shows the center of the topological defects approaching, colliding, and then separating to infinity. Fig. 10(b) shows the pair colliding multiple times. As time $t \to \infty$, the field approaches zero.

In the last case, Fig. 10(c) is the most intricate. The pair approach each other, collide, stay trapped, separate, and then collide again. Initially, it appears that a bion formation is occurring, but suddenly, they separate and move to infinity after the second bounce.

The process can be clearly seen in Fig. 11. Before the collision, for $0 \leq t \leq 33$, the center of the field remains constant at 1.0. After the collision, the field value fluctuates slightly around 1.0. These fluctuations represent another way to store energy, aside from kinetic energy: the energy of the discrete bound mode called shape mode. Here's how it happens: the pair accumulates a significant amount of kinetic energy before the collision. After the first collision, most of this kinetic energy is converted into shape mode energy. As the distance between the pair decreases, the force between them increases, leading to another collision where the energy of the shape mode is converted back into kinetic energy. If the kinetic energy is sufficient, the pair can overcome the attraction force and separate to infinity.

It was observed in (CAMPBELL; SCHONFELD; WINGATE, 1983) that this phenomenon does not occur for every initial velocity. Surprisingly, when studying the initial velocity, a critical velocity v_c is found, above which reflection always occurs. Below v_c, bion formation predominates. In the intermediate velocity region, the resonance phenomenon emerges.

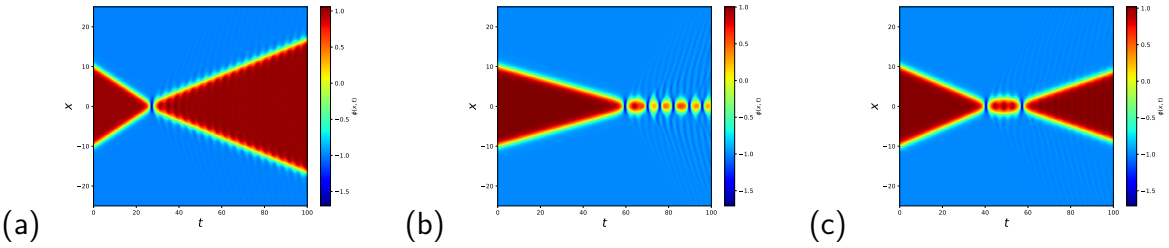

Figure 10 – (a) Reflection for $v_{\text{in}} = 0.350$, (b) bion formation for $v_{\text{in}} = 0.150$, and (c) two-bounce solution for $v_{\text{in}} = 0.228$. Source: The Author (2024).

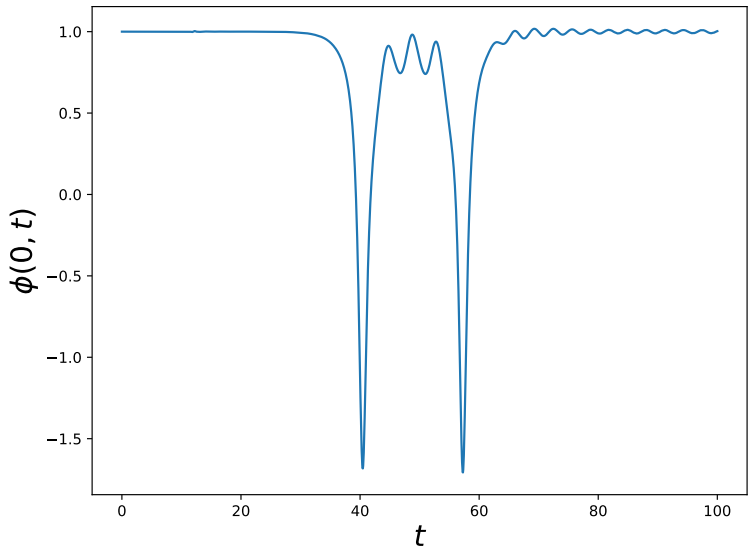

Figure 11 – Center of the field as a function of time for $v_{\text{in}} = 0.228$. Source: The Author (2024).

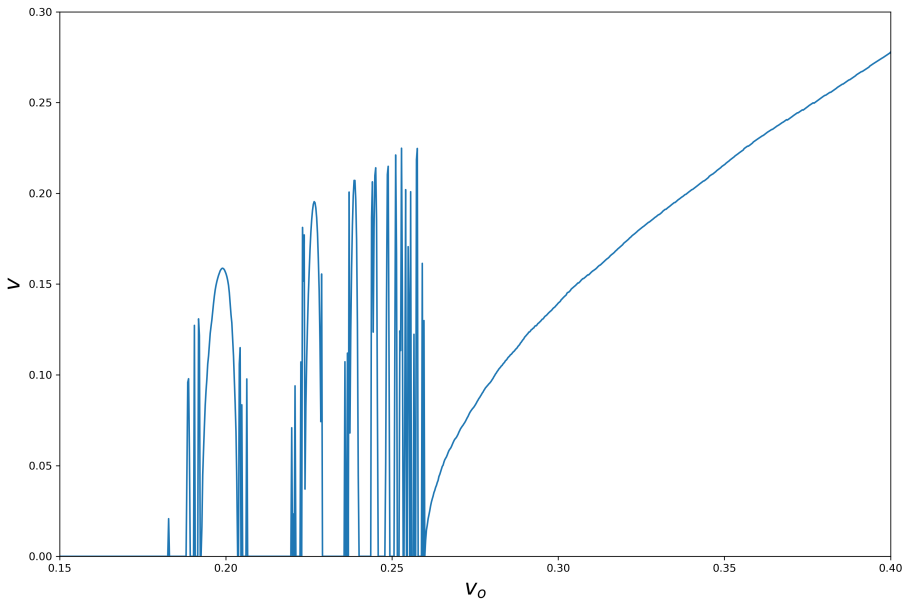

Figure 12 – Final velocity as a function of initial velocity. Source: (CAMPBELL; SCHONFELD; WINGATE, 1983).

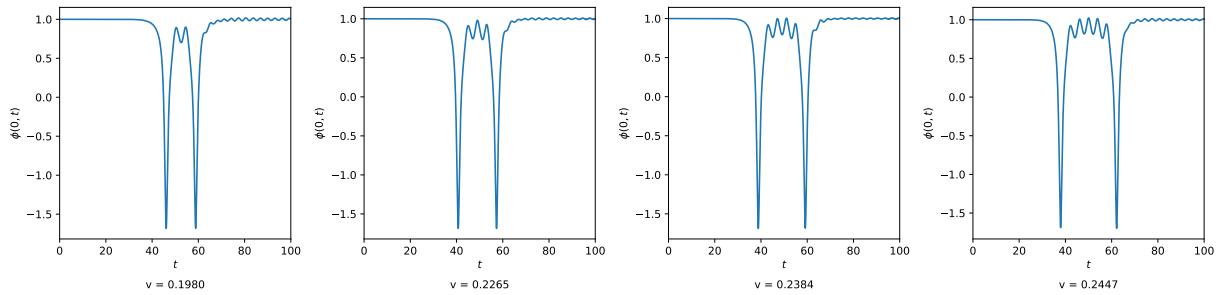

Figure 13 – The center of the field as function of time for some values of initial velocity. Source: The Author (2024).

The final velocity as a function of the initial velocity is shown in Fig. 3.1. For the $\lambda\phi^4$ model, the critical velocity v_c is 0.2598. Above this velocity, the energy exchange mechanism is always guaranteed. Since there are no resonance windows for every velocity in the system, there must be another condition on the frequencies for the phenomenon to occur. In (CAMPBELL; SCHONFELD; WINGATE, 1983), it was shown that the frequency with the time between collisions follows a linear relation 3.1.

$$\omega_s T = 2\pi n + \delta. \tag{3.1}$$

The phase δ is chosen to always be within the interval $0 < \delta < 2\pi$, and n in the equation represents the resonance window number.

The profile of the center of the field can be seen in Fig. 13. As we increase the initial velocity, more "fingers" appear in the collision, as can be seen in the first figure of Fig. 13 between $t \approx 48$ and $t \approx 58$. The frequency in 3.1 is the shape mode frequency. There is a very convenient way to find that frequency. If we compute the time between collisions in the resonance windows and the window numbers, the slope of the line connecting the points is $2\pi/\omega_s$.

The result can be seen for the first 8 resonance windows in Fig. 14. The slope of the line is $2\pi/n \approx 5.189$ and $\delta \approx 3.049$. This leads to a resonance frequency of $\omega_s = 1.211$. There is a way to check the integrity of the results we found. By looking at 2.9, we find the theoretical frequency of the kink-antikink bound state by studying perturbations around the kink (antikink) function. The value $\omega_1^2 = \dfrac{3}{2}$ is quite close to the value we found, with an error of around 1%.

By collecting the data, we have found a way to characterize the kink-antikink bound state both theoretically and through numerical experiments. Since the frequency obtained from the

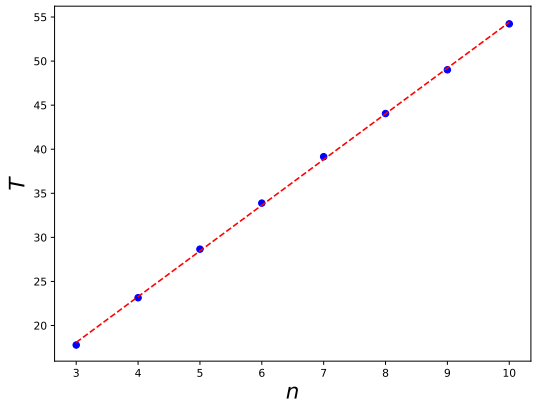

Figure 14 – Time between collisions as a function of the window number. The dots represent the points we collected from the first 8 resonance windows, and the line is the linear regression line. The Author (2024).

theoretical approach is very close to that from the simulations, Fig. 3 shows good agreement between the two eigenfunctions of the kink-antikink resonance bound state.

3.2 SINE-GORDON POTENTIAL

In order to study the difference between the interactions of an integrable model and a non-integrable one, we will examine the sine-Gordon kink-antikink dynamics. The initial conditions are

$$\phi_{\mathrm{K}\bar{\mathrm{K}}}(x,0) = \phi_{\mathrm{K}}[\gamma(x+x_o)] + \phi_{\bar{\mathrm{K}}}[\gamma(x-x_o)] - 2\pi. \tag{3.2}$$

The result of the collision can be seen in Fig. 15. It is interesting to compare it with Fig. 10(a). Firstly, the collision does not generate radiation. This means that the pair does not lose energy, and the initial velocity equals the final velocity. This can be seen by noting that the slope of the line of the center is the same before and after the collision. Independently of the initial velocity we choose, this fact will always occur, and it is guaranteed by the solutions of the linearized potential we described in 2.2. Unlike in Fig. 3.1, the final velocity as a function of the initial velocity is just a straight line $v = v_o$.

Another intriguing effect that is also present in non-integrable models (but not in $\lambda\phi^4$) is the switching of sectors. Initially, the kink-antikink pair is in one of the vacua, connecting 0 to 2π. Ultimately, the pair connects the vacua -2π to 0. The kink-antikink pair can jump to another sector if a theory has more than two vacuum states.

As we have seen, it may seem like the sine-Gordon model does not correspond to any

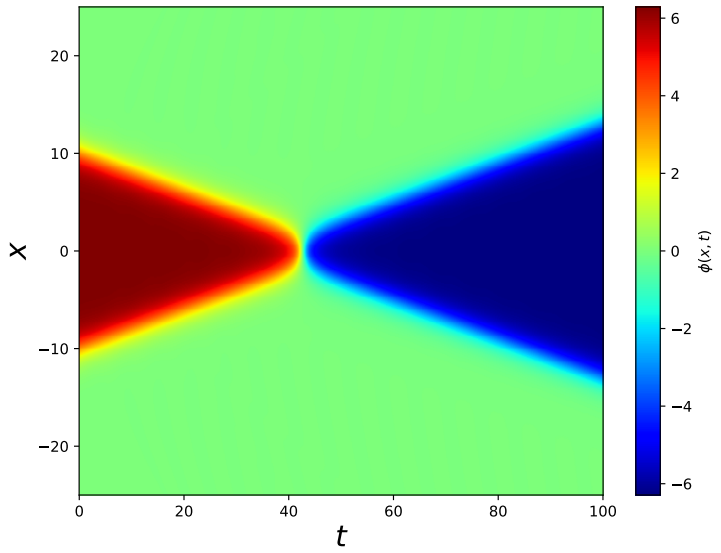

Figure 15 – Kink-antikink collision in the sine-Gordon potential for initial velocity $v = 0.1$. Source: The Author (2024).

realistic physical system since there is no radiation in interactions. However, like $\lambda\phi^4$, the sine-Gordon model is a prototype in physics since it naturally appears in many areas.

The sine-Gordon equation and its properties appear in the Frenkel–Kontorova model for perturbations in crystals (BRAUN; KIVSHAR, 1998), thin superconductors (SWIHART, 1961), and the theoretical study of vortex solutions (BARASHENKOV; PELINOVSKY, 1998) of field theories. More applications are extensively discussed in (CUEVAS-MARAVER; KEVREKIDIS; WILLIAMS, 2014).

3.3 THE ϕ^6 MODEL

Continuing the work we started in 2.3, we will study the interactions between the pair of topological defects. Again, we need to solve the field equations of motion for the potential and kink-antikinks described in 9. Now, as the linearized potentials in 9 are asymmetric, there is a difference between the kink-antikink collision and the antikink-kink one. The initial conditions are given in 2.12.

The collision results can be seen in Fig. 16. The first three collisions show behavior similar to Fig. 10, with the exception that the duration of the phenomena is longer because the initial velocities are smaller. Fig. 16 (c) is similar to Fig. 15 since the sector switching phenomenon occurs. The last image shows a bion formation combined with sector switching: the pair keeps

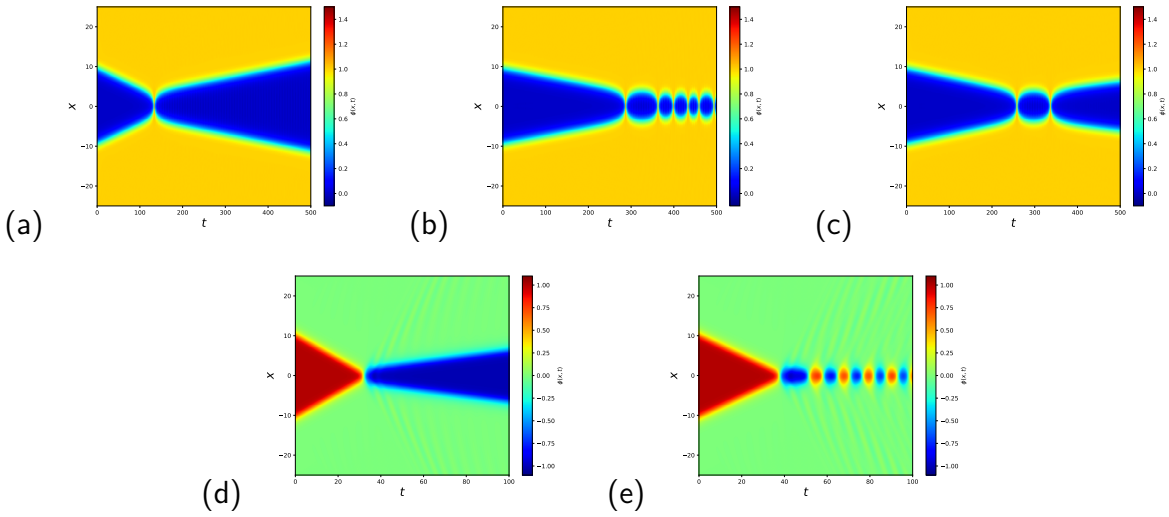

Figure 16 – Antikink-kink solutions: (a) Reflection for $v_{\text{in}} = 0.050$, (b) bion formation for $v_{\text{in}} = 0.027$ and (c) two-bounce solution for $v_{\text{in}} = 0.0228$. Kink-antikink solutions: (d) sector switch for $v_{\text{in}} = 0.300$ and (e) bion formation for $v_{\text{in}} = 0.250$. Source: The Author (2024).

switching between sectors.

The theory we have presented so far must be reviewed at some point. Since the linearized potentials in Fig. 9 do not show any discrete solution different from the zero mode, the interactions should not present resonance windows.

Another point of view arises in (DOREY et al., 2011). The authors showed that the bound mode frequencies are not stored in a single topological defect but in the entire pair. The modes we have seen in (CAMPBELL; SCHONFELD; WINGATE, 1983) are called *localized* modes, and consequently, the modes in the ϕ^6 model are the delocalized ones.

To explain how the phenomena occur, we need to analyze the potential in 2.8. We now have to take derivatives with respect to the combination of kink + antikink or antikink + kink. A combination of the potentials in 9 is reached. Fig. 17 (a) shows the potential for the antikink-kink case and (b) for the kink-antikink case. Viewing the situation as an analogy with quantum mechanics dynamics under a potential well, as can be seen in (GRIFFITHS; SCHROETER, 2018), the kink-antikink case leads us to a barrier where there are no bound states. However, the antikink-kink case with energy $1 < \omega^2 < 4$, as shown in Fig. 17, has bound states.

Fig. 18 supports the discussion above. The antikink-kink case in (a) is characterized by the presence of resonance windows, which can be seen by observing the blue lines. The first bounce is marked by the lowest line, where the value of the field changes abruptly. There are regions where the field changes multiple times, which can be interpreted as bion formation,

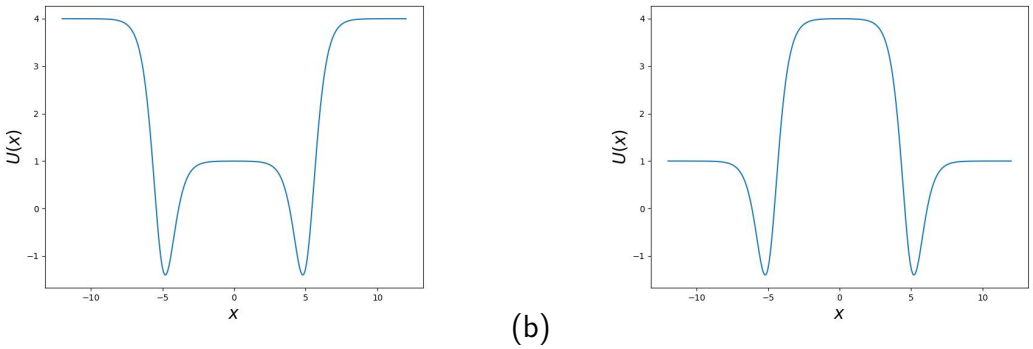

(a) (b)

Figure 17 – Linearized potential for ϕ^6 model. (a) for the antikink-kink collision and (b) for the kink-antikink collision. Source: The Author (2024).

as in Fig. 16 (b), and there are regions where the field changes twice and then returns to its initial value, as in Fig. 16 (c). These are the resonance windows. Finally, there are regions where the field changes abruptly only once, corresponding to the reflection in Fig. 16 (a).

Now Fig. 18 (b) shows the kink-antikink collisions for several initial velocity values. The first thing we notice is the absence of resonance windows, a characteristic of kink-antikink collisions, as mentioned above. Further to the right, the field value changes abruptly to the other vacuum value. It starts at $\phi(0,t) = 1$ and goes to $\phi(0,t) = -1$, which is a sector change that happens only once, as in Fig. 16 (d). The green region is characterized by multiple changes between vacuum values, indicating the bion formation seen in Fig. 16 (e).

The antikink-kink case exhibits resonance windows for small initial velocities, as allowed by the linearized potential. The theoretical process to get eigenfrequencies is different now. Unlike the localized ones, the delocalized modes depend on the distance between the kink and the antikink.

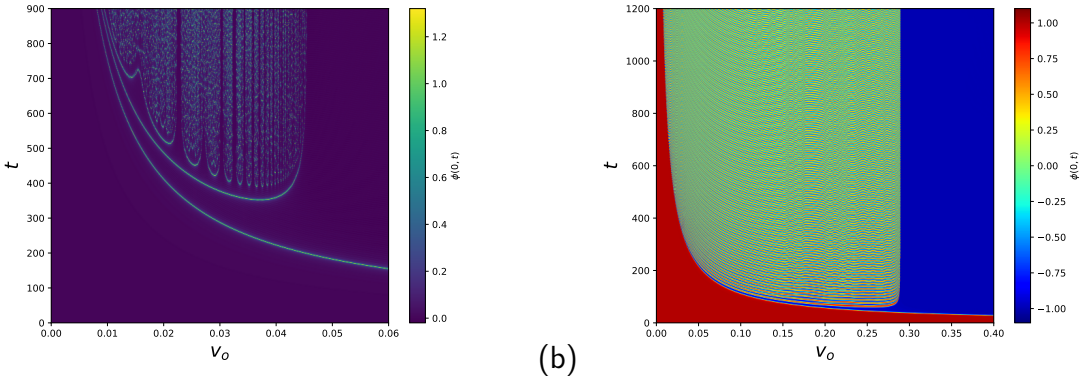

(a) (b)

Figure 18 – Evolution of the center of the field as a function of the initial velocity. (a) antikink-kink and (b) kink-antikink collisions. Source: The Author (2024).

Fig. 19 shows the method that we mentioned). Since there are several modes, the frequency converges to the one with the smaller energy. The vertical line represents the half-separation of the resonance window and allows us to conclude that the theoretical approach aligns with the collision results. Each resonance window has a group of curves, as shown in Fig. 19 (b). The key point is that the resonance frequency is not determined by just one resonance window but by an entire group, as indicated by 3.1. A method to obtain the graph is described in A.2.

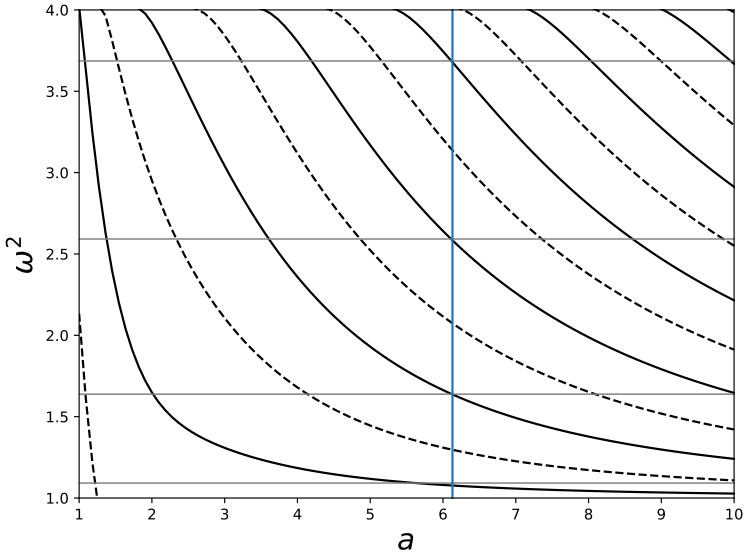

Figure 19 – Frequencies for $v_{\text{in}} = 0.04548$ vs. (b) even (solid) and odd (dashed) bound states for antikink-kink configuration, as a function of the half-separation a. Source:(DOREY et al., 2011).

Fig. 19 also shows the four delocalized frequencies (horizontal lines). Since in the resonance window the half separation distance is $a \approx 6.13$ (blue vertical line), it is possible to check that these frequencies match the first four even solutions. The collision results show the frequency $\omega = 1.0452$, which is very close to the point where the first horizontal line in Fig. 19 is $\omega = 1.045$. The other lines are $\omega = 1.28$, 1.61, and 1.92.

It is important to notice that, although the delocalized modes store energy differently, the way we characterize these modes is very similar to what was done in (CAMPBELL; SCHONFELD; WINGATE, 1983). The linear relation between the time between collisions and the resonance window number is still valid. This is proven by the slight difference between the frequency values, generating an error of less than 0.02%. This result is also promising since we found the curves in Fig. 19 by solving Schrödinger's equation for the linearized potential in Fig. 17,

and the approximations of the field equation we used to derive Schrödinger's equation are sufficiently accurate.

4 ON THE LOCALIZED AND DELOCALIZED MODES IN KINK-ANTIKINK INTERACTIONS: A TOY MODEL

4.1 OVERVIEW

Topological defects are the results of non-linearity that originate from a potential in field theory. There are many kinds of topological defects, always connected to spontaneous symmetry-breaking phenomena (CAMPO; ZUREK, 2014). In (2+1)-dimensional field theories, vortices have significant applications in superconductors (YANAGISAWA; HASE, 2013; YANAGISAWA; HASE; TANAKA, 2018), while in (3+1) theories, skyrmions (KUCHKIN et al., 2020; KUCHKIN et al., 2023; KUCHKIN; KISELEV, 2023) and monopoles (RAJANTIE, 2012) are examples.

The simple kink-antikink pair is found in dislocations in gold (EL-BATANOUNY et al., 1987) and buckled graphene (YAMALETDINOV; SLIPKO; PERSHIN, 2017). Additionally, in condensed matter and crystallography, applications appear in liquid crystals (DELEV et al., 2019; LI; HOU; GAO, 2022; MUNIYAPPAN; RAVICHANDRAN; MANIKANDAN, 2023).

The $\lambda\phi^4$ model discussed earlier exhibits chaotic structures in the interactions between its topological defects (CAMPBELL; SCHONFELD; WINGATE, 1983). The shape mode obtained by the kinks is called a localized mode, as it is stored in the kink and antikink separately. On the other hand, the ϕ^6 model has a different structure in its modes, where the so-called delocalized modes are stored in the pair, as we have seen before.

The method we use to evaluate our results when dealing with delocalized modes differs from the localized ones. More than one localized mode often destroys the resonance windows' structure due to competition between them. Aliakbar et al. (MARJANEH; SIMAS; BAZEIA, 2022) contributed to this scenario, where they constructed a model in which resonance windows arise from more than one localized mode.

Delocalized modes were first studied by Dorey et al. in (DOREY et al., 2011) using the ϕ^6 model. Due to the asymmetry between the kink-antikink and antikink-kink configurations, resonance windows only appear in the antikink-kink configuration. Since there are many modes, the resonance frequency is estimated by a numerical inspection. Each resonance frequency corresponds to a distance between the pair's center in a two-bounce window. Using this, we can construct a graph of the spectral structure ω^2 as a function of the half-separation x_o and determine which mode is stored in the collision.

To explore some properties of delocalized modes, we need to analyze the linearized potential of the pair. However, solving the Schrödinger-like equation with that potential is difficult, as there are only a few potentials with analytic solutions. To study these properties, we build a ϕ^2 toy model. Since the derivatives that appear in the linearized potential are second-order in the field, we will obtain potential wells like those in quantum mechanics and apply their properties.

4.2 THE MODEL

We will work with a field theory described by 1.1. The potential is a piecewise ϕ^2 described by 4.1.

$$V(\phi) = \begin{cases} \dfrac{A^2}{2}\phi^2, & 0 < \phi < \phi_1, \\ -\dfrac{B^2}{2}(\phi - \phi_o)^2 + V_+, & \phi_1 < \phi < \phi_2, \\ \dfrac{C^2}{2}(\phi - \lambda)^2, & \phi > \phi_2. \end{cases} \tag{4.1}$$

The potential was built to have three minima, like the ϕ^6 potential, which means there are two different topological sectors. The continuity of the potential leads us to a well-behaved function and also solutions of the equations of motion that are piecewise well-behaved functions. By using the methods of 1.9 and applying the potential 4.1, we obtain the following solution for a kink in the sector $(0, 1)$

$$\phi_{\mathsf{K}}(x) = \begin{cases} e^{Ax}, & x < x_1, \\ \phi_0 + K\sin[B(x - x_1) + \theta_0], & x_1 < x < x_2, \\ \lambda + (\phi_2 - \lambda)e^{-C(x - x_2)}, & x > x_2. \end{cases} \tag{4.2}$$

The potential 4.1 has eight parameters that we still need to discuss. By requiring continuity of the potential and its derivative at the points $\phi = \phi_1$ and $\phi = \phi_2$, we can eliminate four of the quantities and express V_+, ϕ_1, ϕ_2, and λ, which means that only A, B, C, and ϕ_0 are indeed free parameters. By making a rescaling of units, i.e., $x^\mu \to B^{-1}\phi_0^{-1}x^\mu$, the quantities B and ϕ_0 can be merged into a single one, which we set to 1. This means that our model has only two free parameters, A and C.

Finally, the piecewise equations 4.2 also have four new constants x_1, x_2, θ_0, and K. By working with the continuity of the function and its derivative at points $x = x_1$ and $x = x_2$, all of these four quantities can be expressed as functions of the free parameters A and C. The

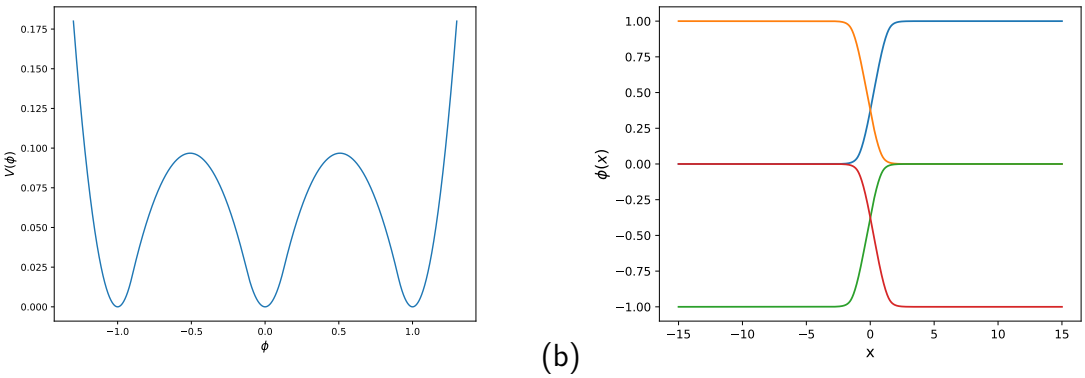

(a) (b)

Figure 20 – The piecewise functions. (a) the potential and (b) the four topological defects. The values are $A = \sqrt{3}$ and $B = 2$. Source: (SANTOS; CAMPOS; MOHAMMADI, 2024).

relation between the quantities can be found in appendix C. The other topological defects can be written as functions of the kink $\phi_{\mathrm{K}}(x) = \phi_{(0,1)}(x)$ as follows: $\phi_{(1,0)}(x) = \phi_{(0,1)}(-x)$, $\phi_{(0,-1)}(x) = -\phi_{(0,1)}(x)$, and $\phi_{(-1,0)}(x) = -\phi_{(0,1)}(-x)$. All four topological sectors, as well as the potential, can be seen in Fig. 20.

4.3 STABILITY EQUATION

Searching for fluctuations like 2.7 in the kink solution, we obtain a Schrödinger-like equation with the linearized potential given by the second derivative of 4.1. Since the potential is a piecewise ϕ^2, the linearized potential will also be a piecewise one with constant functions. Then we obtain a finite square well in the form

$$U(x) = \begin{cases} A^2, & x < x_1, \\ -1, & x_1 < x < x_2, \\ C^2, & x > x_2. \end{cases} \tag{4.3}$$

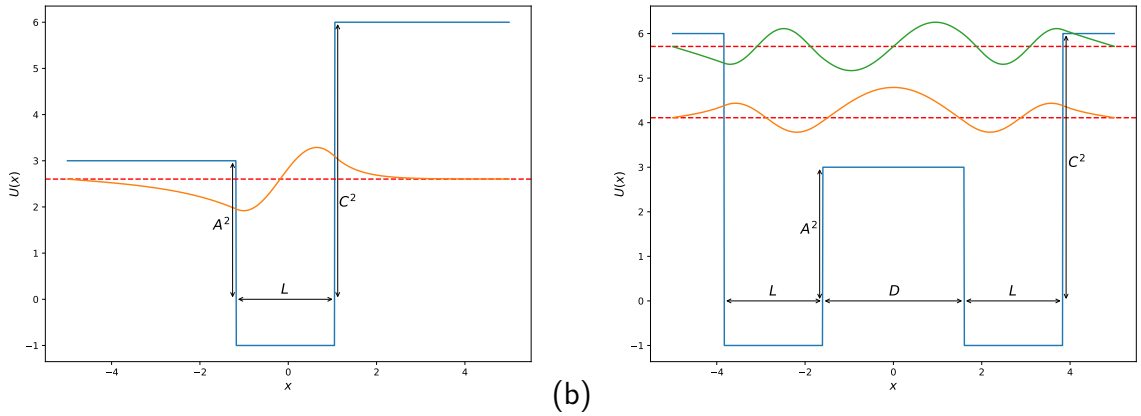

(a) (b)

Figure 21 – The linearized potentials. (a) kink (b) pair. The parameters are $A = \sqrt{3}$ and $C = \sqrt{6}$. Source: (SANTOS; CAMPOS; MOHAMMADI, 2024).

Otherwise, when we work with the entire pair and study the delocalized modes, the linearized potential is given by

$$U(x) = \begin{cases} C^2, & x < -\dfrac{D}{2} - L, \\ -1, & -\dfrac{D}{2} - L < x < -\dfrac{D}{2}, \\ A^2, & -\dfrac{D}{2} < x < \dfrac{D}{2}, \\ -1, & \dfrac{D}{2} < x < \dfrac{D}{2} + L, \\ C^2, & x > \dfrac{D}{2} + L. \end{cases} \tag{4.4}$$

Both linearized potentials are shown in Fig. 21.

For localized modes, the square-well potential, described in 4.3, gives solutions of interest in the region $0 \leq \omega < A$ in the case $C > A$ and $0 < \omega < C$ otherwise. Solutions with $\omega > C(A) > A(C)$ do not describe the bound localized states.

Since the square well is easily solvable, the eigenfunctions $\eta(x)$ can be found by using the functions in D, their continuities, and continuities in their derivatives. It is possible to reach a transcendental equation for the eigenfrequency spectrum, given by 4.5, with $k_1 = \sqrt{A^2 - \omega^2}$, $k_2 = \sqrt{1 + \omega^2}$, and $k_3 = \sqrt{C^2 - \omega^2}$.

A profile of the potential for the parameters $A = \sqrt{3}$ and $C = \sqrt{6}$ can be found in Fig. 21 (a). As we are interested in different scenarios for the number of localized modes, changing the values of A and C allows us to control the number of modes that fit in the potential. The number of modes as a function of the parameters A and C can be found in Fig. 22.

$$\tan(k_2 L) = \frac{k_2(k_1 + k_3)}{k_2^2 - k_1 k_3} \tag{4.5}$$

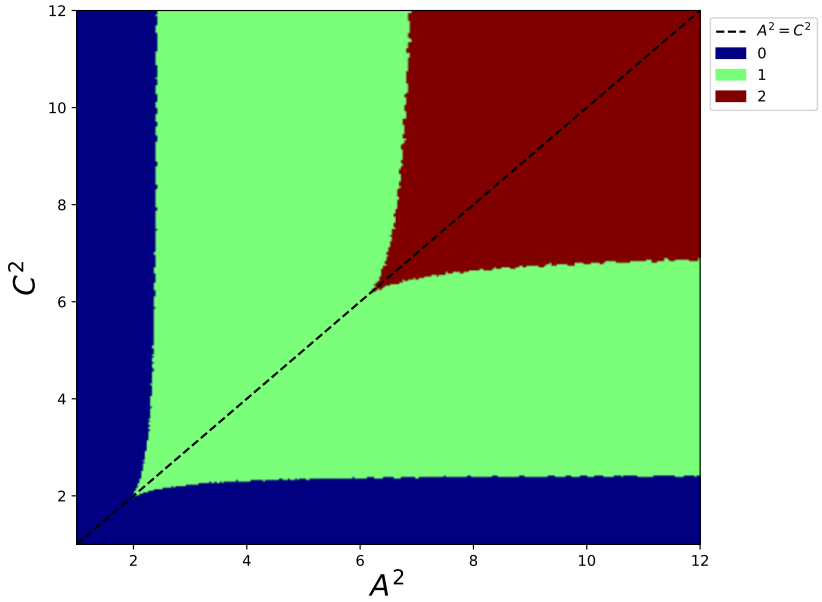

Figure 22 – Number of modes as function of A and C. The dotted line shows the number of modes for $A = C$ Source: (SANTOS; CAMPOS; MOHAMMADI, 2024).

Since the transcendental equation is symmetric under the transformations $A \to C$ and $C \to A$, Fig. 22 is also symmetric with respect to the line $A^2 = C^2$. The blue region represents the region with only the trivial zero mode solution, while the green and red regions correspond to one and two modes, respectively.

It is interesting to understand the limits of the square well. If $C \to \infty$, we reach a semi-infinite square well with the transcendental equation

$$\tan(k_2 L) = -\frac{k_2}{k_1}, \tag{4.6}$$

that agrees with the well-known problem. Looking at the line $A^2 = C^2$, we reach a symmetric finite square well satisfying the transcendental equation $\tan(k_2 L) = \dfrac{2k_1 k_2}{k_2^2 - k_1^2}$, with both symmetric and antisymmetric solutions.

Changing the scenario, Fig. 21 (b) shows the delocalized modes potential. The shape of the potential is essential to the problem. If the height A is greater than C, we reach a situation similar to the ϕ^6 model with kink-antikink collisions, as seen in Fig. 17 (b). This means that only cases where $C > A$ are of interest. Furthermore, we need to work only in the region $A < \omega < C$.

Taking the solutions in D and considering the continuity of the eigenfunction and its derivative, we obtain two different transcendental equations for the eigenfrequencies: one for the even solutions and the other for the odd ones. The equations below represent the transcendental

equations for the even and odd solutions, respectively.

$$\begin{cases} \tan\left(k_1\dfrac{D}{2}\right) = \dfrac{\frac{k_3}{k_1} - \frac{k_2}{k_1}\tan(k_2L)}{1 + \frac{k_3}{k_2}\tan(k_2L)} \\ \tan\left(k_1\dfrac{D}{2}\right) = \dfrac{\frac{k_1}{k_2}\left[1 + \frac{k_3}{k_2}\tan(k_2L)\right]}{\tan(k_2L) - \frac{k_3}{k_2}} \end{cases} \tag{4.7}$$

The $\frac{D}{2}$ factor in 4.7 is the half separation distance between the pair.

Equations 4.7 also allow an interesting analysis of the limiting cases. If we make $C \to \infty$, we reach the infinite square well with a small perturbation at the center. Therefore, the bound frequencies can be expanded in powers of A^2 in the following form

$$\omega_n^2 = \frac{n^2\pi^2}{(D+2L)^2} - 1 + A^2\left[\frac{D}{D+2L} - \frac{1}{n\pi}\sin\left(\frac{n\pi D}{D+2L}\right)\right] + \mathcal{O}(A^4) \tag{4.8}$$

Now we have all we need to numerically solve the equations of motion for the kink-antikink (antikink-kink) collisions and study the results. That is what we will do in the next section.

4.4 KINK-ANTIKINK AND ANTIKINK KINK COLLISIONS

As we already know, initial conditions are needed to solve the partial differential equations. For the kink-antikink case, we initiate the collision with

$$\begin{cases} \phi(x,0) = \phi_{\mathsf{K}}[\gamma(x+x_0)] + \phi_{\bar{\mathsf{K}}}[\gamma(x-x_0)] - 1, \\ \dot{\phi}(x,0) = -\gamma v\left\{\phi'_{\mathsf{K}}[\gamma(x+x_0)] - \phi'_{\bar{\mathsf{K}}}[\gamma(x-x_0)]\right\}, \end{cases} \tag{4.9}$$

and for antikink-kink case

$$\begin{cases} \phi(x,0) = \phi_{\mathsf{K}}[\gamma(x-x_0)] + \phi_{\bar{\mathsf{K}}}[\gamma(x+x_0)], \\ \dot{\phi}(x,0) = -\gamma v\left\{-\phi'_{\mathsf{K}}[\gamma(x-x_0)] + \phi'_{\bar{\mathsf{K}}}[\gamma(x+x_0)]\right\}. \end{cases} \tag{4.10}$$

In order to explore the scenarios we want, we need to adjust the parameters A and C properly. If we choose the pair $(A,C) = (p_1,p_2)$ to obtain a number n_{D} of delocalized modes in the antikink-kink collision analysis, to get the same number of modes when analyzing the kink-antikink scenario, it is necessary to change the values to $(A,C) = (p_2,p_1)$. This is needed because we know that the number of modes depends on the depth of the well, and switching from kink-antikink to antikink-kink also changes the heights of the potential.

We need to use the linear relation between the time between collisions and the number of resonance windows 3.1 to obtain the frequencies of the vibrational modes excited in the

collisions. The phase δ has the same condition as before, in the interval $(0, 2\pi)$. Then, we can define an error by comparing the numerical frequency with the theoretical one from the transcendental equation for localized modes. The relative error can be estimated as

$$\delta\omega = \frac{|\omega_{\text{theoretical}} - \omega_{\text{collision}}|}{\omega_{\text{theoretical}}}. \tag{4.11}$$

For delocalized modes, a graphical construction will be presented.

4.4.1 $(A^2, C^2) = (8/3, 8/3)$

The most common case in the literature occurs when there is only one localized mode, as in (CAMPBELL; SCHONFELD; WINGATE, 1983). The possible scenarios for the kink-antikink and antikink-kink collisions can be seen in Fig. 23. The case where we choose $A^2 = C^2 = 8/3$ is particularly special because we reach a symmetric square well in Fig. 21(a) that matches precisely with the one in (CAMPOS; MOHAMMADI, 2020).

More details of the collision results can be seen in Fig. 24. We interpret the graphs similarly to what we did in the ϕ^6 model, except that in the kink-antikink case, there is a new feature: we can see something like a resonance window. There are regions where the field changes abruptly twice and then returns to its initial value, as in Fig. 23(c). It means that we can also use what we saw in the $\lambda\phi^4$ model to determine the resonance frequencies of such windows.

Fig. 24 (a) shows the kink-antikink collision, while (b) shows the antikink-kink collision. The first thing we notice is that the resonance windows in the kink-antikink scenario are thinner than those in the antikink-kink case. Another characteristic of the kink-antikink collision is the higher critical velocity, especially when there is more than one localized mode or a mixture of localized and delocalized modes. This leads us to believe there is competition between these modes, disrupting the multi-resonance windows' chaotic structure.

The theoretical approach involves measuring the time between collisions for resonance windows in Fig. 24, which allows us to find the resonance frequencies through 4.5 since there is only one localized mode. The calculated frequency is $\omega_{\mathsf{T}} = 1.533$. For the antikink-kink case, we obtain a frequency of $\omega_{\bar{K}K} = 1.500$, and for the kink-antikink case, the frequency is $\omega_{K\bar{K}} = 1.499$. The associated error for both cases is practically the same, around 0.55%.

From now on, we also need to account for the discontinuity between the values of A and C. A larger difference between A and C leads to a greater discontinuity in the linearized potentials, which also contributes to numerical errors.

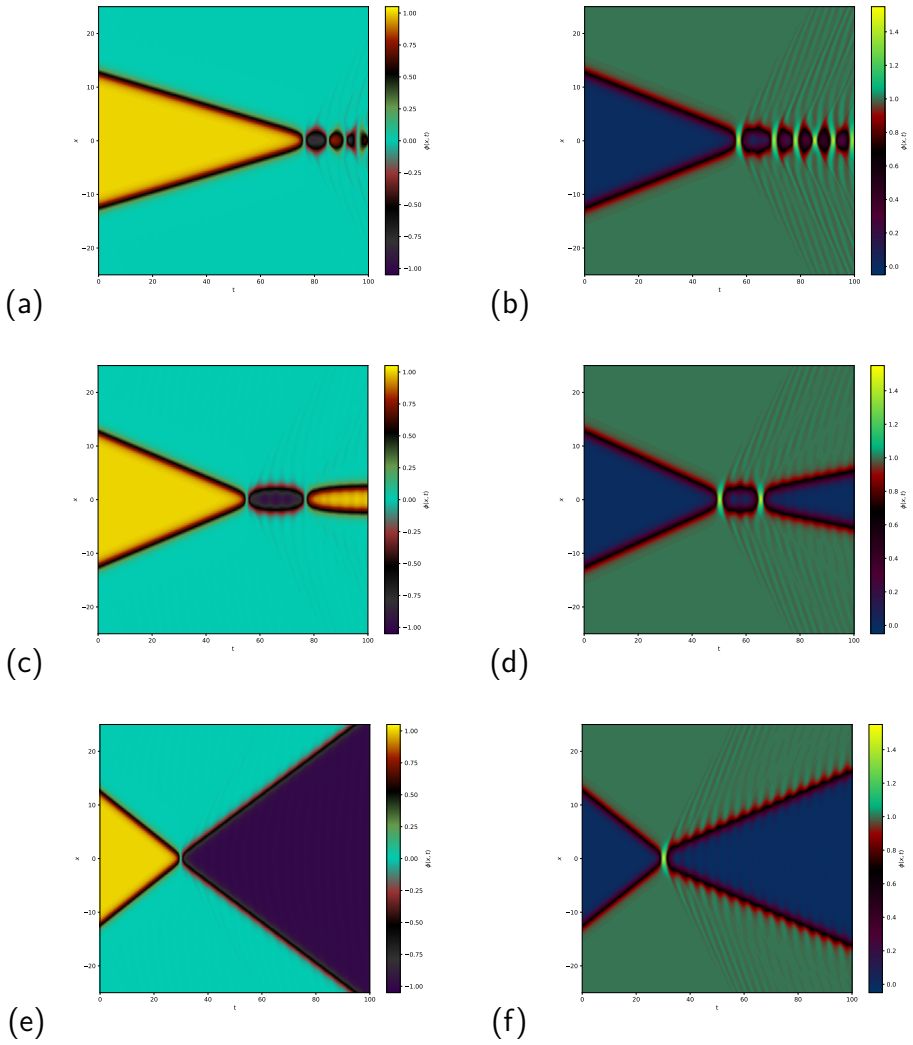

Figure 23 – Bion formation in (a) an kink-antikink with $v_o = 0.15$, and (b) a antikink-kink collision with $v_o = 0.2$. Two-bounce window for (c) a kink-antikink with $v_o = 0.211$, and (d) an antikink-kink collision with $v_o = 0.23$. Reflection for (e) a kink-antikink with $v_o = 0.40$, and (f) an antikink-kink collision with $v_o = 0.4$. Parameters are $A^2 = C^2 = 8/3$. Source: (SANTOS; CAMPOS; MOHAMMADI, 2024).

4.4.2 $(A^2, C^2) = (1.5, 7.0)$

We will now examine the case where there are only delocalized modes. This case is similar to the ϕ^6 model in (DOREY et al., 2011), achieved by setting the parameters as $A^2 = 1.5$ and $C^2 = 7.0$. The center of the field as a function of time and initial velocity can be seen in Fig. 25.

In addition to the thinner resonance windows in the kink-antikink case, the critical velocity is higher than in the antikink-kink scenario. Although the system has the same configuration as the ϕ^6 model, we can look at Fig. 25(a) and observe the resonance structure, indicating

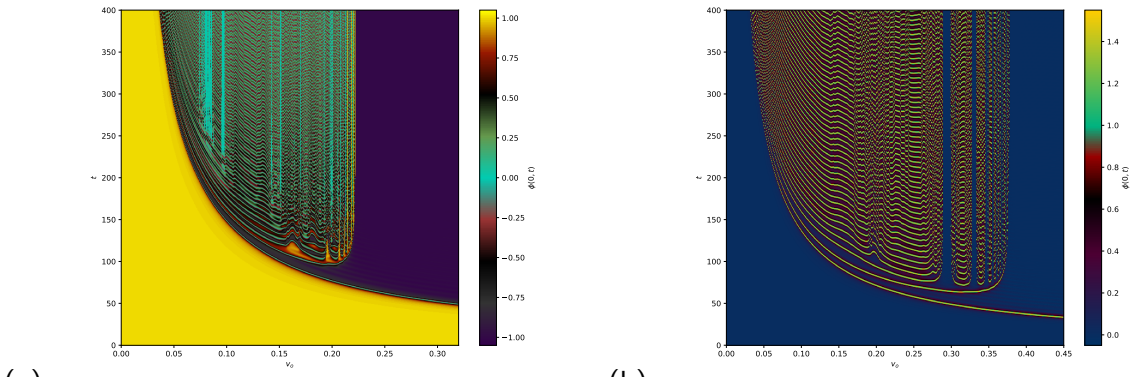

(a) (b)

Figure 24 – Center of the field as function of time and initial velocity. The collisions cases are (a) kink-antikink (b) antikink-kink. The parameters are $A^2 = C^2 = 8/3$. Source: (SANTOS; CAMPOS; MOHAMMADI, 2024).

that the pair continues exchanging energy between the vacua.

The numerical simulations gives the frequencies $\omega_{\bar{K}K} = 1.381$ and $\omega_{K\bar{K}} = 1.371$. The difference between the frequencies has become larger now and we believe that is due to the radiation from the sector changing. The spectrum for both cases is shown in Fig. 26.

Since the linearized potential for both cases in Fig. 21 is the same, the lines are also identical for both cases, and this fact will persist in future analyses. In both Fig. 26 (a) and (b), the resulting frequency falls within the area of the lines, indicating that a good approximation has been achieved through our methods. The kink-antikink case also shows a larger separation between the pair. This is because the resonance windows in the kink-antikink case typically occur at higher initial velocities than in the antikink-kink case. A higher initial velocity implies more incredible kinetic energy, leading to a larger separation.

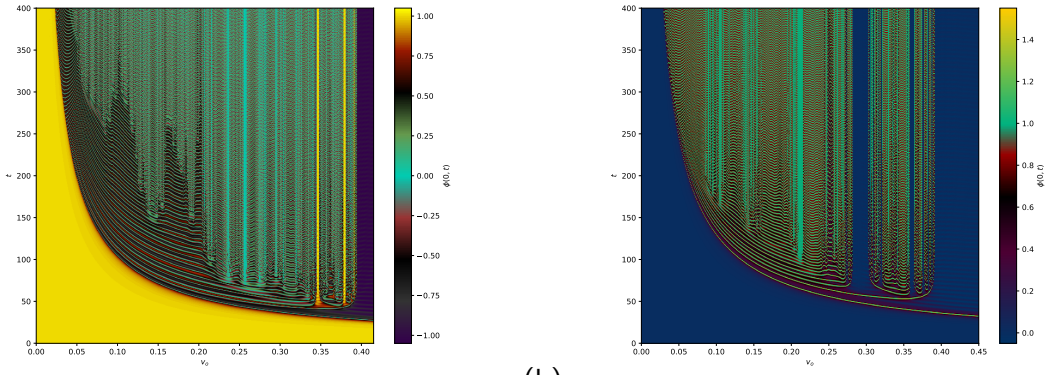

(a) (b)

Figure 25 – Center of the field as a function of time and initial velocity. The collisions cases are (a) kink-antikink (b) antikink-kink. The parameters are $A^2 = 1.5$ and $C^2 = 7.0$. Source: (SANTOS; CAMPOS; MOHAMMADI, 2024).

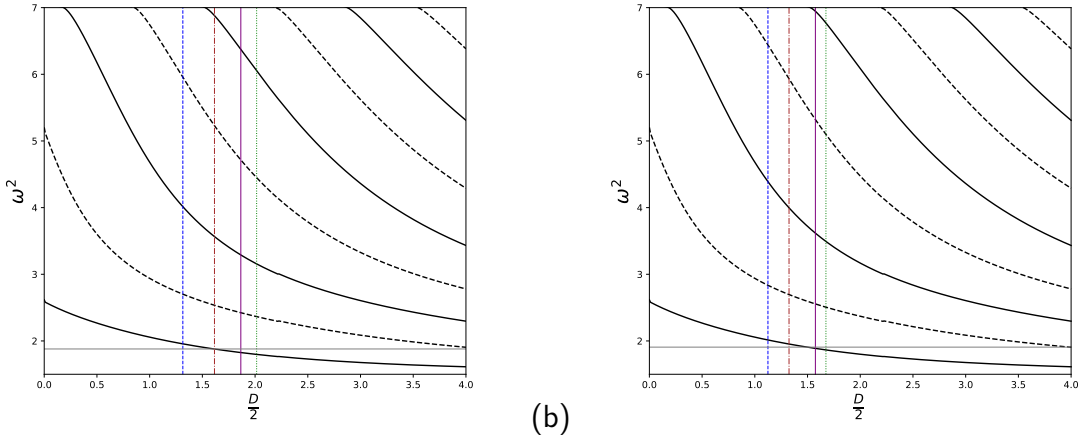

(a) (b)

Figure 26 – Spectrum of interactions in the collisions. The scenarios are (a) kink-antikink and (b) antikink-kink. The parameters are $A^2 = 1.5$ and $C^2 = 7.0$. Source: (SANTOS; CAMPOS; MOHAMMADI, 2024).

4.4.3 $(A^2, C^2) = (2.5, 6.125)$

It is time to mix the modes. Until now, the state of the art has focused on systems with only localized or delocalized modes. Our model can combine both. The first case we analyze is achieved by setting the parameters to $(A^2, C^2) = (2.5, 6.125)$. The profile of the center of the field as a function of initial velocity and time can be seen in Fig. 27. Notably, the critical velocity for the antikink-kink case is still smaller than for the kink-antikink case. In the kink-antikink case, for $v_o \approx 0.375$, it is possible to observe a triple bounce with a sector-changing phenomenon.

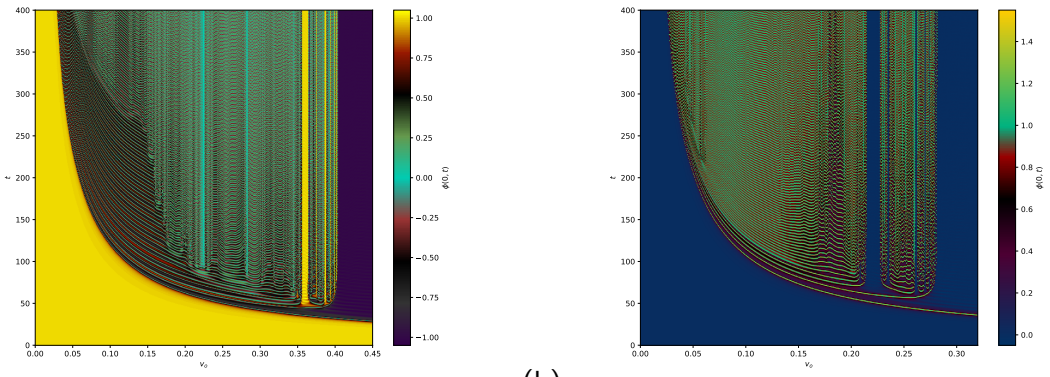

(a) (b)

Figure 27 – Center of the field as a function of time and initial velocity. The collisions cases are (a) kink-antikink (b) antikink-kink. The parameters are $A^2 = 2.5$ and $C^2 = 6.125$. Source: (SANTOS; CAMPOS; MOHAMMADI, 2024).

For these parameters, the transcendental equations provide a theoretical resonance frequency of localized modes $\omega_{\mathsf{T}} = 1.563$. Since there is a mixture of modes, it is interesting to check what frequency the system will present. By studying the resonance windows in Fig. 27, we obtain $\omega_{\mathsf{K}} = 1.528$ and $\omega_{\mathsf{K}} = 1.501$.

The associated errors are $\delta\omega_{\mathsf{K}} = 2.1\%$ and $\delta\omega_{\mathsf{K}} = 4.0\%$. Regarding the delocalized modes, Fig. 28 shows the spectrum as a function of the half separation distance of the pair $D/2$. The modes start only at $A \approx 1.581$, so there is no horizontal line in the spectrum graph in Fig. 28.

Finally, the first line in Fig. 28 is an odd mode. This occurs because quantum systems bound in a symmetric potential always have the lowest eigenfunction as an even one. Therefore, the localized mode is symmetric, and the first delocalized mode is asymmetric.

4.4.4 $(A^2, C^2) = (6.05, 6.05)$

The next case is the one where $A^2 = C^2 = 6.05$. This case presents two localized modes and no delocalized ones. The transcendental equation gives us two solutions: $\omega_{\mathsf{T}_1} = 1.678$ and $\omega_{\mathsf{T}_2} = 2.457$. However, Fig. 29 shows the center of the field as a function of time and initial velocity, and it is clear that the resonance windows are suppressed in both cases. This situation is common in the literature, although there are a few exceptions (DOREY et al., 2021b; MARJANEH; SIMAS; BAZEIA, 2022).

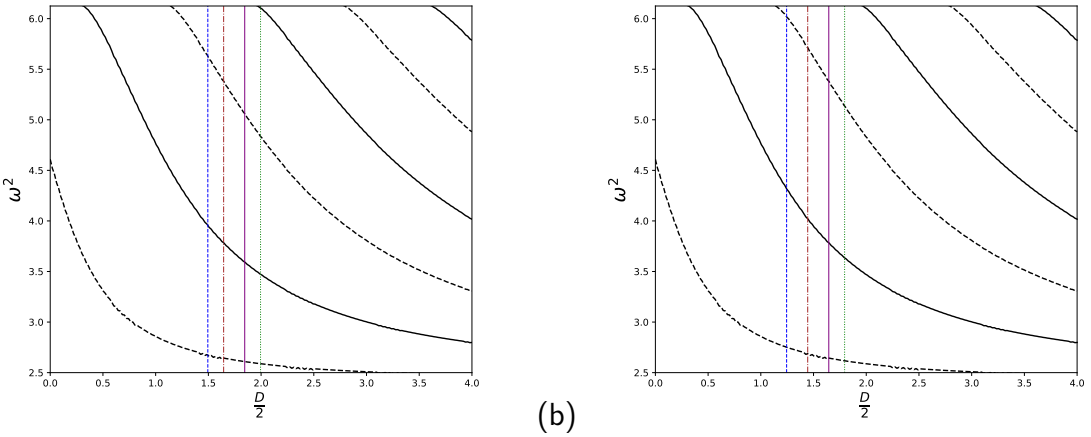

(a) (b)

Figure 28 – Spectrum of interactions in the collisions. The scenarios are (a) kink-antikink and (b) antikink-kink. The parameters are $A^2 = 2.5$ and $C^2 = 6.125$. Source: (SANTOS; CAMPOS; MOHAMMADI, 2024).

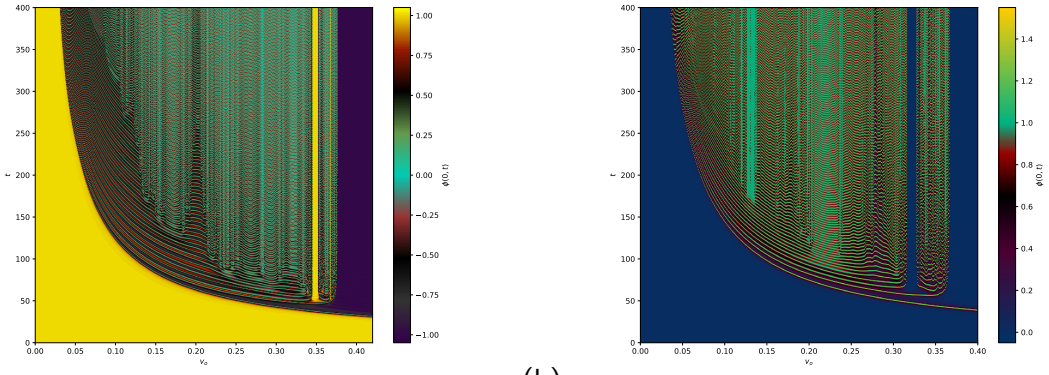

(a) (b)

Figure 29 – Center of the field as a function of time and initial velocity. The collisions cases are (a) kink-antikink (b) antikink-kink. The parameters are $A^2 = C^2 = 6.025$. Source: (SANTOS; CAMPOS; MOHAMMADI, 2024).

Despite the resonance windows in Fig. 29 being suppressed, it is still possible to determine the system's resonance frequency by examining the false resonance windows, intervals of initial velocity where the system nearly exhibits a resonance window. In these intervals, the pair gains a significant amount of energy but not enough to separate to infinity. The presence of the second localized mode creates competition between modes.

The resonance frequency from the simulations is $\omega_{\bar{K}K} = 1.588$, while in the kink-antikink scenario, even the false resonance windows are absent, consistent with the windows being thinner whenever they do appear. The associated error is then $\delta\omega_{\bar{K}K} = 5.2\%$.

4.4.5 $(A^2, C^2) = (1.5, 9.0)$

Now, we will add to the cases where the number of localized modes equals two. From the previous section, we already know that the localized resonance windows are suppressed. By adding delocalized modes, the situation becomes even worse.

Fig. 32 shows the center of the fields as a function of time and initial velocity. While the profile of the curves appears similar, they are actually quite different.

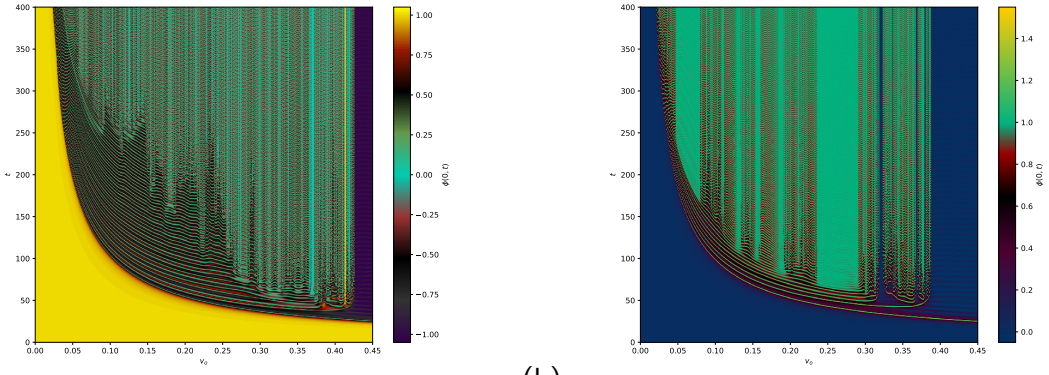

(a) (b)

Figure 30 – Center of the field as a function of time and initial velocity. The collisions cases are (a) kink-antikink (b) antikink-kink. The parameters are $A^2 = 1.5$ and $C^2 = 9.0$. Source: (SANTOS; CAMPOS; MOHAMMADI, 2024).

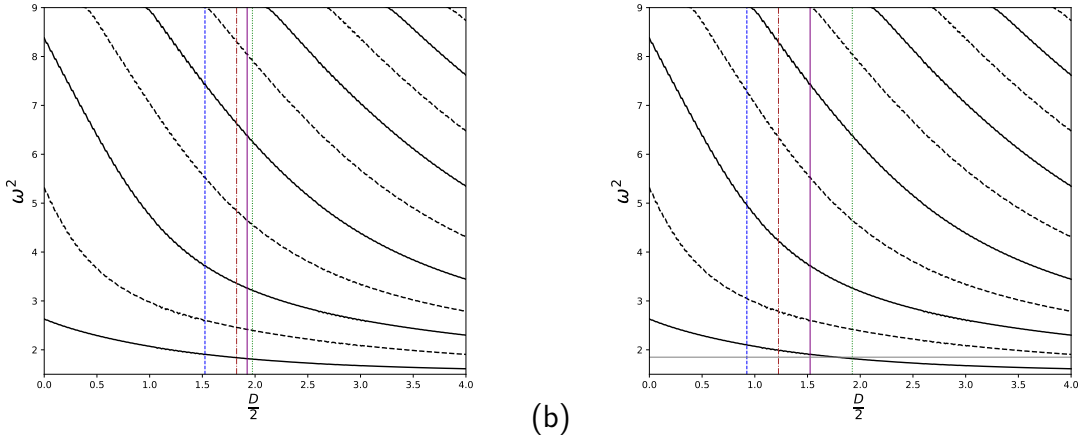

(a) (b)

Figure 31 – Spectrum of interactions in the collisions. The scenarios are (a) kink-antikink and (b) antikink-kink. The parameters are $A^2 = 1.5$ and $C^2 = 9.0$. Source: (SANTOS; CAMPOS; MOHAMMADI, 2024).

In the kink-antikink case, the resonance windows are suppressed, while in the antikink-kink case, the windows are thinner than those in the previous similar case $(A^2, C^2) = (1.5, 7.0)$.

This leads us to conclude that the addition of delocalized modes can also disturb the structure of resonance windows, as was previously known to happen with localized modes. Since the resonance structure in the kink-antikink case is more fragile due to the sector-changing phenomena, the windows are suppressed.

The collisions provide a frequency of $\omega_{\bar{K}K} = 1.358$, and the spectrum in Fig. 31(b) shows that the result is in good agreement with this structure. In that range of inter-kink distances, the numerical frequency is indeed compatible with the lowest delocalized mode.

4.4.6 $(A^2, C^2) = (7.0, 9.5)$ and $(A^2, C^2) = (7.0, 12.0)$

Now, let us add to the cases in which the number of localized modes is equal to two. We already know from the previous section that the localized resonance windows are suppressed. By adding delocalized modes, the structure that was already messy due to localized modes becomes even worse in this sense.

Fig. 32 shows the center of the fields as a function of time and initial velocity. The profile of the curves seems to be the same, but they are quite different.

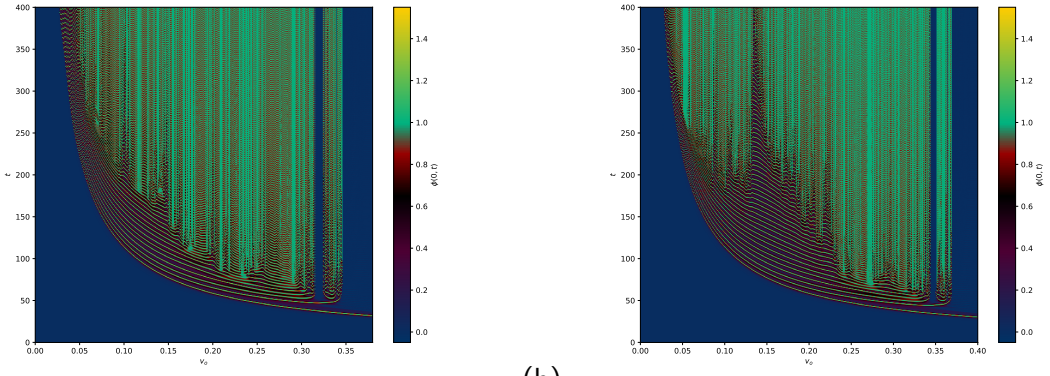

(a) (b)

Figure 32 – Center of the field as a function of time and initial velocity for antikink-kink collisions. The parameters are (a) $A^2 = 7.0$ and $C^2 = 9.5$ (b) $A^2 = 7.0$ and $C^2 = 12.0$. Source: (SANTOS; CAMPOS; MOHAMMADI, 2024).

In Fig. 32 (a), a few resonance windows and many false ones are visible. This allows us to calculate the resonance frequency, which is $\omega_{\bar{K}K} = 1.563$. The transcendental equation approach provides two theoretical frequencies: $\omega_{\mathsf{T}_1} = 1.697$ and $\omega_{\mathsf{T}_2} = 2.624$. This indicates that our predictions converge to the lowest frequency mode with an error of $\delta\omega_{\mathsf{T}} = 7\%$. We

can now affirm that the system converges to the resonance frequency of the lowest frequency (energy), even if the resonance frequency is reached through false resonance windows.

In Fig. 32 (b), the scenario shows a fully suppressed resonance structure, even in the antikink-kink case. While a few resonance windows were found, they were not sufficient to ensure acceptable accuracy. This suggests that the additional delocalized modes destroyed the resonance window structure.

4.4.7 $(A^2, C^2) = (2.7, 9.5)$

Finally, the last case emphasizes the influence of delocalized modes in cases with only one localized mode. The profile of the center of the field is presented in Fig. 33. The kink-antikink case gets its resonance windows fully suppressed, so we will not calculate the frequency in such cases. The result is expected since we saw in previous sections the effect of the addition of delocalized modes, and the kink-antikink resonance structure is more fragile than the antikink-kink scenario.

The antikink-kink case presents a theoretical frequency of $\omega_{\mathsf{T}} = 1.596$ and a collision frequency of $\omega_{\bar{K}K} = 1.548$ so we can estimate the error $\delta\omega_{\bar{K}K} = 3\%$. The delocalized modes start at $A \approx 1.643$, which is far from the collision frequency. Therefore, our results reinforce the notion that the lowest vibrational mode primarily governs the appearance of resonance windows.

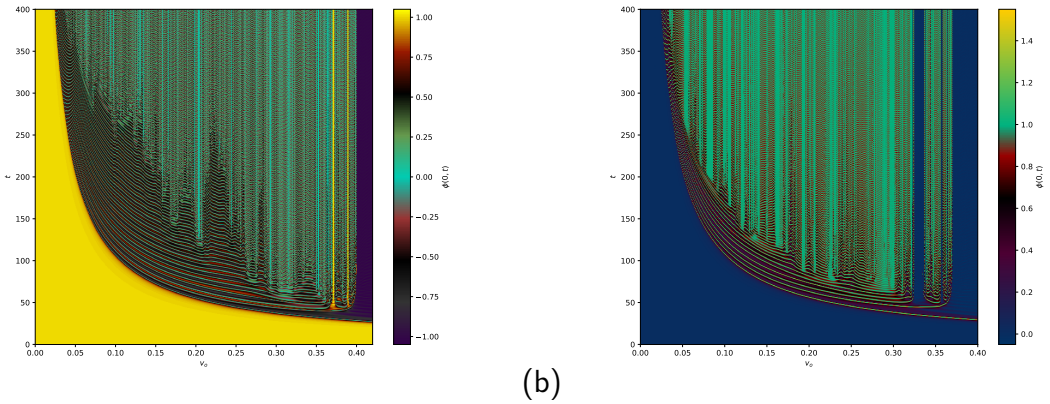

(a) (b)

Figure 33 – Center of the field as a function of time and initial velocity. The collisions cases are (a) kink-antikink (b) antikink-kink. The parameters are $A^2 = 2.7$ and $C^2 = 9.5$. Source: (SANTOS; CAMPOS; MOHAMMADI, 2024).

4.5 CONCLUSION

In this work, we have constructed a ϕ^2 piecewise potential to help understand localized and delocalized modes' role in the resonance structure of kink and antikink interactions. When small perturbations around static solutions are studied, the toy model leads to an asymmetric square well potential. The model has two controllable parameters, A and C, which allow us to change the heights of the asymmetric square well and obtain more modes of each kind.

Since the potential has three minima, the kink-antikink case presents a sector change with resonance windows, i.e., intervals of initial velocity where the pair switches the sector and comes back multiple times. On the other hand, the antikink-kink case shows a resonance structure very similar to what we observe in the $\lambda\phi^4$ model, the expected resonance structure. Notably, in both scenarios, the resonance frequency converges to the lowest level of the energy spectrum.

Collisions with one localized mode or a few delocalized ones present a rich resonance structure, similar to (CAMPBELL; SCHONFELD; WINGATE, 1983) and (DOREY et al., 2011). Our results show that when we increase the number of modes, whether localized or delocalized, the resonance structure becomes narrower until it is suppressed. This happens because even if the system exhibits the lowest frequency, other modes are not negligible when the energy is redistributed after the collision process. The frequent occurrence of resonance windows suggests that higher-frequency modes are only weakly excited. However, these modes can become significantly excited, suppressing any resonant behavior.

The model helps also to understand the radiation emitted after kink and antikink interactions, as it allows for the study of detailed scenarios with and without sector switching, while keeping all linear features of the model fixed. This can be done by measuring the amount of radiation that reaches the boundary at infinity after the interaction.

5 FINAL REMARKS

In this work, we have explored the phenomenon of resonance windows in kink and antikink interactions. These phenomena occur in $(1+1)$-dimensional field theory and arise from the properties of the potential function $V(\phi)$.

In chapter 1, we examined the fundamental aspects of the field theories of interest. The linearity of the wave equation can be disrupted by nonlinear phenomena due to the addition of a function on the right-hand side. We discussed essential concepts such as energy, action, and how static solutions can emerge from the BPS condition.

Chapter 2 focused on understanding the potentials. We identified two principal properties that potentials must satisfy: they must be positive-definite and even functions. These properties allow for the existence of topological defects, which were discussed in this chapter, along with the kink and antikink pairs related to the potentials we consider.

Topological defects serve as particle-like solutions, meaning their energy density is localized. These objects can also interact with each other, exhibiting attractive interactions between kink and antikink pairs, while kink-kink and antikink-antikink pairs repel each other. By examining small perturbations around the static solutions, we arrive at a Schrödinger-like equation. The solution $\omega = 0$ is always guaranteed due to the system's translational symmetry. Discrete solutions ($\omega \neq 0$) represent bound states, whereas continuum solutions correspond to radiation.

In chapter 3, we focused on the numerical results of interactions between kink and antikink pairs. Three possible outcomes emerge from these interactions: first, a reflection where the kink-antikink (or antikink-kink) pair interacts and escapes to infinity separately; second, a collision leading to annihilation, known as bion formation.

Additionally, the pair can interact, collide, separate, collide again, and then separate to infinity. This scenario lies between reflection and bion formation and can be explained through the energy exchange mechanism. This mechanism involves an exchange between kinetic and shape mode energy, allowing the pair to remain in a bound state for a while before separating. The range of initial velocities for which this occurs is termed resonance windows, with shape modes referred to as localized modes.

All these scenarios are observed in the $\lambda\phi^4$ theory. In contrast, while ϕ^6 theory also exhibits these scenarios, they differ significantly. In the $\lambda\phi^4$ theory, the shape mode is localized within

each topological defect, whereas in the ϕ^6 model, the mode is distributed across the entire pair, leading to the concept of delocalized modes. Furthermore, antikink-kink collisions exhibit phenomenology similar to that of $\lambda\phi^4$, while kink-antikink interactions have unique features, including the sector change phenomenon, where the pair transitions to another topological sector.

Finally, chapter 4 presents a toy model for studying localized and delocalized modes. In this model, we created a $V \sim \phi^2$ piecewise potential that yields a square well as the stability potential in the linearized regime. With two free parameters, A and C, representing the height of the square well, we can introduce more localized or delocalized modes or even a mixture of them.

Our results align with the $\lambda\phi^4$ and ϕ^6 models. When only one localized mode is present, the resonance structure is rich, as seen in (CAMPBELL; SCHONFELD; WINGATE, 1983). Adding more localized modes can disrupt this structure due to competition among modes. In contrast, a few localized modes remain consistent with (DOREY et al., 2011), presenting a rich resonance structure, but adding more delocalized modes may also compromise the resonance structure due to mode competition.

In conclusion, both localized and delocalized modes can influence the resonance windows, indicating that even higher modes must be considered when discussing energy distribution among the various possible modes.

A DISCRETIZATION METHODS FOR DIFFERENTIAL EQUATIONS

$$\frac{\partial^2}{\partial t^2}\phi(x,t) - \frac{\partial^2}{\partial x^2}\phi(x,t) + b(x)\frac{\partial}{\partial t}\phi(x,t) = f(x), \tag{A.1}$$

In order to solve problems like A.1 and in 3, we need to study a few methods to assist us in that task. We will not show all methods, but the problems we solved here have been addressed using the methods described below. First of all, we need to present the numerical language we are going to use here. On a computer, there is no way to represent an infinite spacetime grid. Instead, we solve problems within a box of length $2L$ (from $-L$ to $+L$) in space and T in time. This means that the x-axis will be divided into N_x points and the time-axis into N_t points, leading to small intervals between two subsequent points of $dx = 2L/N_x$ and $dt = T/N_t$.

Instead of working with a field $\phi(x,t)$, we are going to work with a field in points x_i and t_j of spacetimes, like $\phi(x_i, t_j)$ where i is the space index, $i = 0, 1, ..., N_{x-1}$ and j the time index, $j = 0, 1, ..., N_{t-1}$. So, the field configuration in the point (x_i, t_j) can be expressed as $\phi_{i,j}$. That process is called the discretization of the spacetime grid.

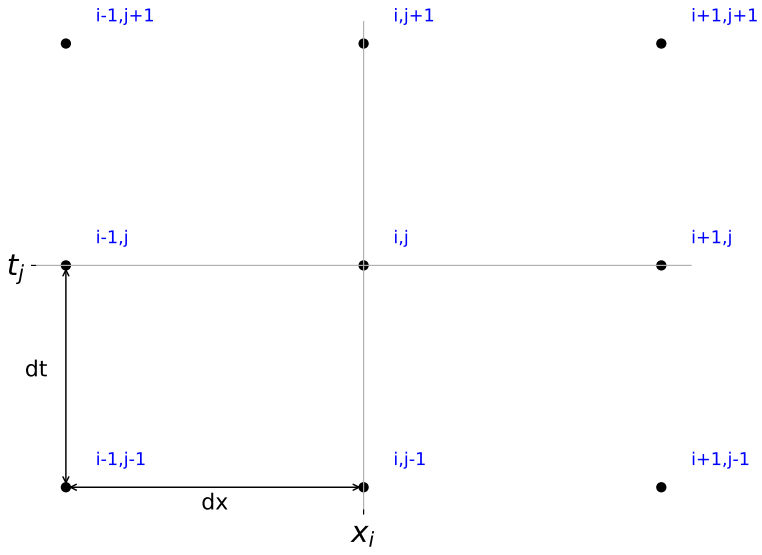

Figure 34 – Spacetime grid. Source: the Author (2024).

Furthermore, setting limits on the spacetime grid can introduce some finite-size problems, so we need to develop techniques to minimize these effects. Since our problem involves radiation, the waves generated at specific points may travel to the box's walls and then reflect back, influencing our field solutions.

A.1 FINITE DIFFERENCES METHOD FOR PDE

To solve the differential equations, we need to teach the computer how to compute derivatives. The simplest method is the finite difference method, which follows the usual definition of derivatives given in mathematics A.2. If the intervals dx and dt are sufficiently small, this method provides a good approximation. Finite difference methods are helpful for problems with discontinuities, as the derivatives depend on only a few points, minimizing the associated error.

$$\begin{cases} \dfrac{\partial}{\partial x}\phi_{i,j} \approx \dfrac{\phi_{i+1,j}-\phi_{i,j}}{dx} + \mathcal{O}(dx) \quad \text{or} \quad \dfrac{\partial}{\partial x}\phi_{i,j} \approx \dfrac{\phi_{i+1,j}-\phi_{i-1,j}}{2dx} + \mathcal{O}(dx), \\ \dfrac{\partial}{\partial t}\phi_{i,j} \approx \dfrac{\phi_{i,j+1}-\phi_{i,j}}{dt} + \mathcal{O}(dt) \quad \text{or} \quad \dfrac{\partial}{\partial t}\phi_{i,j} \approx \dfrac{\phi_{i,j+1}-\phi_{i,j-1}}{2dt} + \mathcal{O}(dt), \end{cases} \tag{A.2}$$

In second-order derivatives we reach

$$\begin{cases} \dfrac{\partial^2}{\partial x^2}\phi_{i,j} \approx \dfrac{\phi_{i+1,j}-2\phi_{i,j}+\phi_{i-1,j}}{dx^2} + \mathcal{O}(dx^2), \\ \dfrac{\partial^2}{\partial t^2}\phi_{i,j} \approx \dfrac{\phi_{i,j+1}-2\phi_{i,j}+\phi_{i,j-1}}{dt^2} + \mathcal{O}(dt^2). \end{cases} \tag{A.3}$$

We can then transform a partial differential equation into an algebraic one by using the boundary conditions to obtain the previous values of the field. Let us begin with equation A.1. By inserting the discretization

$$\frac{\phi_{i,j+1}-2\phi_{i,j}+\phi_{i,j-1}}{dt^2} + b_i\frac{\phi_{i,j+1}-\phi_{i,j-1}}{2dt} = \frac{\phi_{i+1,j}-2\phi_{i,j}+\phi_{i-1,j}}{dx^2} + f_i, \tag{A.4}$$

reorganizing the equation leads to

$$\phi_{i,j+1} = \frac{2}{\alpha_+}(1-\lambda^2)\phi_{i,j} - \frac{\alpha_-}{\alpha_+}\phi_{i,j-1} + \frac{\lambda^2}{\alpha_+}(\phi_{i+1,j}+\phi_{i-1,j}) + \frac{dt^2}{\alpha_+}f_i, \tag{A.5}$$

where $\alpha_\pm = 1 \pm \dfrac{b_i}{2}dt$ and $\lambda = \dfrac{dt}{dx}$. We will use initial conditions as A.6.

$$\begin{cases} \phi(x,0) = \eta(x) \longrightarrow \phi_{i,0} = \eta_i \\ \dot{\phi}(x,0) = \psi(x) \longrightarrow \dot{\phi}_{i,0} = \psi_i \end{cases} \tag{A.6}$$

Thus, it is possible to rewrite A.5 for $t = 0$ using the derivative $\dfrac{\phi_{i,1}-\phi_{i,-1}}{2dt} \approx \psi_i$

$$\phi_{i,1} = (1-\lambda^2)\phi_{i,0} + dt\alpha_-\psi_i + \frac{\lambda^2}{2}(\phi_{i+1,0}+\phi_{i-1,0}) + \frac{dt^2}{2}f_i, \tag{A.7}$$

The equation A.7 gives us the first step towards solving the partial differential equation. By knowing $\phi_{i,1}$, we can continue the iterative process until we have the field solution at every point on the spacetime grid.

The function $b(x)$ is called a bump function, essential for minimizing error. Since our collisions between kinks and antikinks generate radiation, it is crucial that this radiation does not return and alter the field. The bump function acts as a wall that absorbs the radiation near the boundary of the interval. An example of a bump function is A.8.

$$b(x) = \begin{cases} 5e^{\left(1-\frac{10^2}{10^2-x^2}\right)}, & -10 < x < 10, \\ 0, & \text{otherwise.} \end{cases} \tag{A.8}$$

A.1.1 Python Implementation

Using Python 3.12.4, it is possible to implement the algorithm in the following way

```
def solver(phi0, phi0t, dV, L, x, t,v_o, gamma, lamb, nx, nt, dt, dx):
    #EDP SOLVER
    phi_old = np.zeros(nx) #phi_i-1
    phi = np.zeros(nx) #phi_i
    phi_new = np.zeros(nx) #phi_i+1

    field = np.zeros((int(nx/e),int(nt/E)))
    #field function initialization

    for i in range(0,nx):
        phi[i] = phi0(x[i], gamma)
        I = int(i/e)
        if i%e == 0:
            field[I,0] =  phi[i]
            #phi(x,0) = initial condition
    alfa = 1 + dt*bump(x[0])
    beta = 1/alfa
    value = (beta/(1+beta))*(2*(1-lamb*lamb)*phi[0] + lamb*lamb*(phi[nx-1] + phi
        [1]) + 2*dt*phi0t(x[0], gamma, v_o) - dt*dt*dV(phi[0]) + dt*bump(x[0])*
        phi[0])

    phi_old[0] = phi[0]
    phi_new[0] = value
    field[0,1] = value
    #first step

    for i in range(1,nx):
    #next steps
        alfa = 1 + dt*bump(x[i])
        beta = 1/alfa
        value = (beta/(beta+1))*(2*(1-lamb*lamb)*phi[i] + lamb*lamb*(phi[i-1] +
            phi[(i+1)%nx]) + 2*dt*phi0t(x[i], gamma, v_o) - dt*dt*dV(phi[i]) +
```

```
            bump(x[i])*dt*phi[i])
        phi_old[i] = phi[i]
        phi_new[i] = value
        I = int(i/e)
        if i%e == 0:
            field[I,1] = value
    for i  in range(1,nx):
        phi[i] = phi_new[i]
        #field update


    for j in range(2,nt):
    #solving for all times
        alfa = 1 + dt*bump(x[0])
        beta = 1/alfa
        value = beta*(2*(1-lamb*lamb)*phi[0] + lamb*lamb*(phi[nx-1] + phi[1]) -
            phi_old[0] - dt*dt*dV(phi[0]) +  bump(x[0])*dt*phi[0])
        phi_old[0] = phi[0]
        phi_new[0] = value
        J = int(j/E)
        if j%E == 0:
            field[0,J] = value
        for i in range(1,nx):
            alfa = 1 + dt*bump(x[i])
            beta = 1/alfa
            value = beta*(2*(1-lamb*lamb)*phi[i] + lamb*lamb*(phi[i-1]+phi[(i+1)%
                nx]) - phi_old[i] - dt*dt*dV(phi[i]) + bump(x[i])*dt*phi[i])
            phi_old[i] = phi[i]
            phi_new[i] = value
            I = int(i/e)
            J = int(j/E)
            if i%e == 0 and j%E == 0:
                field[I,J] = value

        for k in range(0,nx):
            phi[k] = phi_new[k]
            #field update

    return field
    #returning solution
```

The code above solves the partial differential equation for the field using finite difference methods. It is suitable for field solutions with high precision. In cases where $N_t > 10^5$, the calculations are performed at all points, but the field is only saved after every 25 time steps. This approach ensures high precision while optimizing memory usage.

A.1.2 Five Points Stencil for PDE

There are other ways to discretize derivatives. For problems involving smooth linearized potentials, the Five Points Stencil discretization provides a better approach.

$$\frac{\partial^2}{\partial x^2}\phi_{i,j} \approx \frac{-\phi_{i+2,j} + 16\phi_{i+1,j} - 30\phi_{i,j} + 16\phi_{i-1,j} - \phi_{i-2,j}}{12dx^2} + \mathcal{O}(dx^4). \tag{A.9}$$

The point at which we want to calculate the derivative has a greater weight than the other five points. This method is helpful since the error is of order $\mathcal{O}(dx^4)$. There is no need to change the time evolution discretization because the program's error is small.

By using A.9 in A.1, we reach similar expressions like A.5 and A.7

$$\begin{cases} \phi_{i,j+1} = \frac{2}{\alpha_+}\phi_{i,j} - \frac{\alpha_-}{\alpha_+}\phi_{i,j-1} + \frac{\lambda^2}{12\alpha_+}[-(\phi_{i+2,j} + \phi_{i-2,j}) + 16(\phi_{i+1,j} + \phi_{i-1,j}) - 30\phi_{i,j}] - \frac{dt^2}{\alpha_+}f_i, \\ \phi_{i,1} = \phi_{i,0} + \alpha_- dt\psi_i + \frac{\lambda^2}{24}[-(\phi_{i+2,0} + \phi_{i-2,0}) + 16(\phi_{i+1,0} + \phi_{i-1,0}) - 30\phi_{i,0}] - \frac{dt^2}{2}f_i, \end{cases} \tag{A.10}$$

following the same initial value problem as in A.6. The Python implementation of the discretization described in A.10 is similar to the one we saw for the finite differences method, changing only the mathematical expression for time evolution.

A.2 FINITE DIFFERENCE METHOD FOR EIGENVALUE PROBLEM

We plan to solve the Schrödinger-like equation A.11

$$\left(-\frac{d^2}{dx^2} + U(x)\right)\eta(x) = E\eta(x). \tag{A.11}$$

It is also possible to solve the problem using finite differences discretization. By using the finite difference method to approximate the second-order derivatives, as given in equation A.3, we calculate the equation at point x_i.

$$-\left(\frac{\eta_{i+1} - 2\eta_i + \eta_{i-1}}{dx^2}\right) + U_i\eta_i = E\eta_i \longrightarrow \left(\frac{2}{dx^2} + U_i\right)\eta_i - \frac{(\eta_{i+1} + \eta_{i-1})}{dx^2} = E\eta_i. \tag{A.12}$$

It is possible to see A.12 as an eigenvalue problem of a matrix

$$\begin{bmatrix} \frac{2}{dx^2}+U_0 & -\frac{1}{dx^2} & 0 & 0 & ... & 0 \\ -\frac{1}{dx^2} & \frac{2}{dx^2}+U_1 & -\frac{1}{dx^2} & 0 & ... & 0 \\ 0 & -\frac{1}{dx^2} & \frac{2}{dx^2}+U_2 & -\frac{1}{dx^2} & ... & 0 \\ 0 & 0 & -\frac{1}{dx^2} & \frac{2}{dx^2}+U_3 & ... & 0 \\ \vdots & \vdots & \vdots & \vdots & \ddots & -\frac{1}{dx^2} \\ 0 & 0 & 0 & 0 & ... & \frac{2}{dx^2}+U_{N_x-1} \end{bmatrix} = E\eta_i \qquad \text{(A.13)}$$

All we have to do is diagonalize the matrix in A.13.

A.2.1 Python Implementation

Taking the Numpy library of Python, we can use the functions *diag* and *eigh* to build the Hamiltonian A.13.

```
    def diagonal(V, dx, N):
2   return np.diag(V + (2 / (dx**2)) * np.ones(N))

4   def off_diagonal(dx, N):
    return -1/(dx**2)*np.ones(N-1)
6
    H = diagonal(V(x), dx, N) + np.diag(off_diagonal(dx, N), k=1) + np.diag(
        off_diagonal(dx, N), k=-1)
8   E, eta = eigh(H)
```

The E in the code is a vector with all eigenvalues, and η is a matrix of eigenfunctions, where each line represents an eigenfunction.

B KINK-ANTIKINK ALGORITHMS

The system kink-antikink by itself has algorithms that we should use once we want to obtain information about the simulation.

B.1 KINK FINAL VELOCITY

Velocity is the time derivative of the position function. As we know from 2, the force between a kink-antikink pair is e^{-2R}, which means that if the pair is well separated, the force is almost zero.

Knowing that, if we are dealing with a pair that goes from -1 to 1 (for example, in the $\lambda\phi^4$ model), the center of the field occurs at $\phi(x,t) = 0$. Thus, we can proceed as follows:

- After a time t_1 following the collision, mark the position x_1 of the center of the kink;
- After a time t_2, mark the position x_2 of the center of the kink again;
- Calculate the distance Δx between the positions x_1 and x_2;
- The velocity is given by $v = \frac{x_2 - x_1}{t_2 - t_1}$.

```
for i in range(N_t-1):
    for j in range(N_x.size-1):
        if field[j,i] > 0 and field[j+1,i] < 0:
            l = (j+1)%x.size
            distance = dx*j + dx*field[j,i]/(field[j,i] - field[l,i]) - L
        if (t3 == 0 and d >= 7 and co < 7):
            x1 = d
            t3 = i + 100
        if i == t3:
            x2 = d
        co = d
v = (x2-x1)/(100*dt)
```

The code marks the position of the field in a position that $\phi(x,t) = 0$ when the distance between the centers of kink-antikink is $d > 7$.

B.2 CONSERVATION OF ENERGY

Estimating errors is an important part of numerical approaches. Since we are working in physics, there is an exciting way to do that by using one of the most important laws we know: energy conservation. Although the problems often involve radiation, the information about radiation is also contained in the resulting field $\phi(x,t)$ from the equations of motion. This means that if we calculate the total energy as a function of time, we obtain the system's total energy, including the energy of the radiation.

If any energy is lost, it is due to the numerical error. Therefore, we have a mechanism to estimate the error in numerical simulations. By using 1.6, we can numerically rewrite the energy at time t as

$$\varepsilon(t) \approx \sum_{i=0}^{N-1} \left[\frac{1}{2}(\partial_x \phi(x_i,t))^2 + \frac{1}{2}(\partial_t \phi(x_i,t))^2 + V(\phi(x_i,t))\right] \cdot dx. \tag{B.1}$$

If the dx is small enough, then B.1 gives us a good approximation for the energy.

B.2.1 Python Implementation

Let us now implement energy conservation in the following form

```
for i in range(Nt-2):
    energy = 0
    for j in range(Nx):
        field_x = (field[(j+1)%Nx,i] - field[j,i])/dx
        field_t = (field[j,i+1] - field[j,i])/dt
        auxiliar = dx*(0.5*field_t + 0.5*field_x + V(field[j,i]))
        energy = energy + auxiliar
    energy_vector[i] = energy
```

The program gives us the energy as a function of time. It is easy for us now to compare the energy at the beginning and at the end of the simulation process.

C CONTINUITY RELATIONS OF THE POTENTIAL AND KINK PARAMETERS

By using the continuity of the potential 4.1, the kink 4.2and its derivatives we reach

$$A^2 = B^2 \frac{(\phi_0 - \phi_1)}{\phi_1}, \tag{C.1}$$

$$V_+ = \frac{1}{2} B^2 [\phi_1(\phi_0 - \phi_1) + (\phi_0 - \phi_1)^2], \tag{C.2}$$

$$\lambda = \frac{2V_+}{B^2(\phi_2 - \phi_0)} + \phi_0, \tag{C.3}$$

$$C^2 = B^2 \frac{(\phi_0 - \phi_2)}{(\phi_2 - \lambda)}, \tag{C.4}$$

$$K = \frac{\sqrt{2V_+}}{B}, \tag{C.5}$$

$$\theta_0 = \sin^{-1}\left[\frac{1}{K}(\phi_1 - \phi_0)\right], \tag{C.6}$$

$$x_1 = \frac{1}{A} \ln \phi_1, \tag{C.7}$$

$$x_2 = x_1 + \frac{1}{B} \sin^{-1}\left(\frac{\phi_2 - \phi_0}{K}\right) - \frac{\theta_0}{B}. \tag{C.8}$$

D SOLUTIONS OF ONE AND TWO ASYMMETRIC SQUARE-WELLS

In the text, we solved the Schrödinger-like equation by using the continuity of the eigenfunction and its derivatives in the region of space, obtaining a transcendental equation for the problem and determining the frequencies. For the localized modes, the momenta in the transcendental equation are $k_1^2 = A^2 - \omega^2$, $k_2^2 = 1 + \omega^2$, and $k_3^2 = C^2 - \omega^2$, and the corresponding eigenfunctions are piecewise.

$$\eta(x) = \begin{cases} Ge^{k_1(x-x_1)}, & x < x_1, \\ H_1 \sin[k_2(x-x_1)] + H_2 \cos[k_2(x-x_1)], & x_1 < x < x_2, \\ Ie^{-k_3(x-x_2)}, & x > x_2. \end{cases} \tag{D.1}$$

where the quantites are obtained imposing continuity of $\eta(x)$ and $\eta'(x)$

$$H_1 = \frac{k_1}{k_2} G, \tag{D.2}$$

$$H_2 = G, \tag{D.3}$$

$$I = G \left\{ \frac{k_1}{k_2} \sin[k_2(x_2 - x_1)] + \cos[k_2(x_2 - x_1)] \right\}. \tag{D.4}$$

and the parameter G can be fixed in order to aquire a normalization of the modes.

To lead with delocalized modes we need to change the momenta k_1 to $k_1^2 = \omega^2 - A^2$. As we have a bigger number of regions the eigenfunction general solution are

$$\eta(x) = \begin{cases} G \exp\left[k_3 \left(x + \frac{D}{2} + L\right)\right], & x < -\frac{D}{2} - L, \\ H_1 \sin\left[k_2 \left(x + \frac{D}{2}\right)\right] + H_2 \cos\left[k_2 \left(x + \frac{D}{2}\right)\right], & -\frac{D}{2} - L < x < -\frac{D}{2}, \\ I \cos(k_1 x), & -\frac{D}{2} < x < \frac{D}{2}, \\ -H_1 \sin\left[k_2 \left(x - \frac{D}{2}\right)\right] + H_2 \cos\left[k_2 \left(x - \frac{D}{2}\right)\right], & \frac{D}{2} < x < \frac{D}{2} + L, \\ G \exp\left[-k_3 \left(x - \frac{D}{2} - L\right)\right], & x > \frac{D}{2} + L. \end{cases} \tag{D.5}$$

Requiring continuity of η and its first derivative, we obtain

$$H_1 = G \left[\frac{k_3}{k_2} \cos(k_2 L) - \sin(k_2 L) \right], \tag{D.6}$$

$$H_2 = G \left[\cos(k_2 L) + \frac{k_3}{k_2} \sin(k_2 L) \right], \tag{D.7}$$

$$I = \frac{G}{\cos(k_1 D/2)} \left[\cos(k_2 L) + \frac{k_3}{k_2} \sin(k_2 L) \right]. \tag{D.8}$$

Likewise, the odd delocalized are expressed as

$$\eta(x) = \begin{cases} G\exp\left[k_3\left(x+\frac{D}{2}+L\right)\right], & x < -\frac{D}{2}-L, \\ H_1\sin\left[k_2\left(x+\frac{D}{2}\right)\right] + H_2\cos\left[k_2\left(x+\frac{D}{2}\right)\right], & -\frac{D}{2}-L < x < -\frac{D}{2}, \\ I\sin(k_1 x), & -\frac{D}{2} < x < \frac{D}{2}, \\ H_1\sin\left[k_2\left(x-\frac{D}{2}\right)\right] - H_2\cos\left[k_2\left(x-\frac{D}{2}\right)\right], & \frac{D}{2} < x < \frac{D}{2}+L, \\ -G\exp\left[-k_3\left(x-\frac{D}{2}-L\right)\right], & x > \frac{D}{2}+L. \end{cases} \tag{D.9}$$

BIBLIOGRAPHY

ADAM, C.; DOREY, P.; MARTíN-CARO, A. G.; HUIDOBRO, M.; OLES, K.; ROMANCZUKIEWICZ, T.; SHNIR, Y.; WERESZCZYNSKI, A. Multikink scattering in the φ^6 model revisited. *Physical Review D*, American Physical Society (APS), v. 106, n. 12, p. 125–142, Dec. 2022. ISSN 2470-0029.

ADAM, C.; OLES, K.; ROMANCZUKIEWICZ, T.; WERESZCZYNSKI, A. Spectral walls in soliton collisions. *Phys. Rev. Lett.*, American Physical Society, v. 122, p. 241601, Jun 2019.

ADAM, C.; OLES, K.; ROMANCZUKIEWICZ, T.; WERESZCZYNSKI, A. Spectral walls in antikink-kink scattering in the φ^6 model. *Phys. Rev. D*, American Physical Society, v. 106, p. 105027, Nov 2022.

BARASHENKOV, I.; PELINOVSKY, D. Exact vortex solutions of the complex sine-gordon theory on the plane. *Physics Letters B*, Elsevier BV, v. 436, n. 1–2, p. 117–124, Sep. 1998. ISSN 0370-2693.

BELENDRYASOVA, E.; GANI, V.; MARJANEH, A.; SAADATMAND, D.; ASKARI, A. A new look at the double sine-gordon kink-antikink scattering. *Journal of Physics: Conference Series*, IOP Publishing, v. 1205, p. 007–012, Apr. 2019. ISSN 1742-6596.

BELENDRYASOVA, E.; GANI, V. A. Resonance phenomena in the ϕ^8 kinks scattering. *Journal of Physics: Conference Series*, IOP Publishing, v. 934, p. 012–059, Dec. 2017. ISSN 1742-6596.

BOGOMOL'NYI, E. B. The stability of classical solutions. 10 1976.

BRAUN, O. M.; KIVSHAR, Y. S. Nonlinear dynamics of the frenkel–kontorova model. *Physics Reports*, Elsevier BV, v. 306, n. 1–2, p. 1–108, Dec. 1998. ISSN 0370-1573.

CAMPBELL, D.; LIAO, Y. Semiclassical analysis of bound states in the two-dimensionalσmodel. *Phys. Rev. D Part. Fields*, American Physical Society (APS), v. 14, n. 8, p. 2093–2116, Oct. 1976.

CAMPBELL, D.; SCHONFELD, J.; WINGATE, C. Resonance structure in kink-antikink interactions in 4 theory. *Physica D: Nonlinear Phenomena*, Elsevier BV, v. 9, n. 1–2, p. 1–32, Oct. 1983. ISSN 0167-2789.

CAMPBELL, D. K.; PEYRARD, M.; SODANO, P. Kink-antikink interactions in the double sine-gordon equation. *Physica D: Nonlinear Phenomena*, Elsevier BV, v. 19, n. 2, p. 165–205, Mar. 1986. ISSN 0167-2789.

CAMPO, A. del; ZUREK, W. H. Universality of phase transition dynamics: Topological defects from symmetry breaking. *International Journal of Modern Physics A*, World Scientific Pub Co Pte Lt, v. 29, n. 08, p. 1430018, Mar. 2014. ISSN 1793-656X.

CAMPOS, J. G. F.; MOHAMMADI, A. Quasinormal modes in kink excitations and kink–antikink interactions: a toy model. *The European Physical Journal C*, Springer Science and Business Media LLC, v. 80, n. 5, May 2020. ISSN 1434-6052.

CAMPOS, J. G. F.; MOHAMMADI, A.; QUEIRUGA, J. M.; WERESZCZYNSKI, A.; ZAKRZEWSKI, W. J. Fermionic spectral walls in kink collisions. *Journal of High Energy Physics*, Springer Science and Business Media LLC, v. 2023, n. 1, Jan. 2023. ISSN 1029-8479.

CARRETERO-GONZáLEZ, R.; CISNEROS-AKE, L.; DECKER, R.; KOUTSOKOSTAS, G.; FRANTZESKAKIS, D.; KEVREKIDIS, P.; RATLIFF, D. Kink-antikink stripe interactions in the two-dimensional sine-gordon equation. *Communications in Nonlinear Science and Numerical Simulation*, Elsevier BV, v. 109, p. 106–123, Jun. 2022. ISSN 1007-5704.

CUEVAS-MARAVER, J.; KEVREKIDIS, P. G.; WILLIAMS, F. *The sine-Gordon Model and its Applications: From Pendula and Josephson Junctions to Gravity and High-Energy Physics*. [S.l.]: Springer International Publishing, 2014. ISSN 2196-0003. ISBN 9783319067223.

DELEV, V. A.; NAZAROV, V. N.; SCALDIN, O. A.; BATYRSHIN, E. S.; EKOMASOV, E. G. Complex dynamics of the cascade of kink-antikink interactions in a linear defect of the electroconvective structure of a nematic liquid crystal. *JETP Letters*, Pleiades Publishing Ltd, v. 110, n. 9, p. 607–612, Nov. 2019. ISSN 1090-6487.

DOREY, P.; GORINA, A.; PERAPECHKA, I.; ROMANCZUKIEWICZ, T.; SHNIR, Y. Resonance structures in kink-antikink collisions in a deformed sine-gordon model. *Journal of High Energy Physics*, Springer Science and Business Media LLC, v. 2021, n. 9, p. 145–185, Sep. 2021. ISSN 1029-8479.

DOREY, P.; GORINA, A.; PERAPECHKA, I.; ROMANCZUKIEWICZ, T.; SHNIR, Y. Resonance structures in kink-antikink collisions in a deformed sine-gordon model. *Journal of High Energy Physics*, Springer Science and Business Media LLC, v. 2021, n. 9, Sep. 2021. ISSN 1029-8479.

DOREY, P.; HALAVANAU, A.; MERCER, J.; ROMANCZUKIEWICZ, T.; SHNIR, Y. Boundary scattering in the φ^4 model. *Journal of High Energy Physics*, Springer Science and Business Media LLC, v. 2017, n. 5, p. 107–112, May 2017. ISSN 1029-8479.

DOREY, P.; MERSH, K.; ROMANCZUKIEWICZ, T.; SHNIR, Y. Kink-antikink collisions in the φ^6 model. *Physical Review Letters*, American Physical Society (APS), v. 107, n. 9, Aug. 2011. ISSN 1079-7114.

EL-BATANOUNY, M.; BURDICK, S.; MARTINI, K. M.; STANCIOFF, P. Double-sine-gordon solitons: A model for misfit dislocations on the au(111) reconstructed surface. *Physical Review Letters*, American Physical Society (APS), v. 58, n. 26, p. 2762–2765, Jun. 1987. ISSN 0031-9007.

GANI, V.; KUDRYAVTSEV, A. Kink-antikink interactions in the double sine-gordon equation and the problem of resonance frequencies. *Physical Review E*, American Physical Society (APS), v. 60, n. 3, p. 3305–3309, Sep. 1999. ISSN 1095-3787.

GANI, V. A.; MARJANEH, A. M.; JAVIDAN, K. Exotic final states in the φ^8 multi-kink collisions. *The European Physical Journal C*, Springer Science and Business Media LLC, v. 81, n. 12, Dec. 2021. ISSN 1434-6052.

GANI, V. A.; MARJANEH, A. M.; SAADATMAND, D. Multi-kink scattering in the double sine-gordon model. *The European Physical Journal C*, Springer Science and Business Media LLC, v. 79, n. 7, p. 620–644, Jul. 2019. ISSN 1434-6052.

GINZBURG, V.; LANDAU, L. On the theory of superconductivity. In: *Collected Papers of L.D. Landau*. [S.l.]: Elsevier BV, 1965. p. 546–568.

GRIFFITHS, D. J.; SCHROETER, D. F. *Introduction to Quantum Mechanics*. [S.l.]: Cambridge University Press, 2018. ISBN 9781107189638.

HIGGS, P. Broken symmetries, massless particles and gauge fields. *Phys. Lett.*, Elsevier BV, v. 12, n. 2, p. 132–133, Sep. 1964.

HOSEINMARDY, S.; RIAZI, N. Inelastic collision of kinks and antikinks in the φ^6 system. *International Journal of Modern Physics A*, World Scientific Pub Co Pte Lt, v. 25, n. 16, p. 3261–3270, Jun. 2010. ISSN 1793-656X.

JACKIW, R.; REBBI, C. Solitons with fermion number $1/2$. *Phys. Rev. D Part. Fields*, American Physical Society (APS), v. 13, n. 12, p. 3398–3409, Jun. 1976.

KUCHKIN, V. M.; BARTON-SINGER, B.; RYBAKOV, F. N.; BLüGEL, S.; SCHROERS, B. J.; KISELEV, N. S. Magnetic skyrmions, chiral kinks, and holomorphic functions. *Physical Review B*, American Physical Society (APS), v. 102, n. 14, Oct. 2020. ISSN 2469-9969.

KUCHKIN, V. M.; KISELEV, N. S. Skyrmions and antiskyrmions in monoaxial chiral magnets. *Physical Review B*, American Physical Society (APS), v. 108, n. 5, Aug. 2023. ISSN 2469-9969.

KUCHKIN, V. M.; KISELEV, N. S.; RYBAKOV, F. N.; BESSARAB, P. F. Tailed skyrmions-an obscure branch of magnetic solitons. *Frontiers in Physics*, Frontiers Media SA, v. 11, Apr. 2023. ISSN 2296-424X.

LI, Y.; HOU, C.; GAO, Y. A continuum model for solitons in the twisted magnetic liquid crystals. *Results in Physics*, Elsevier BV, v. 32, p. 105–122, Jan. 2022. ISSN 2211-3797.

LOHE, M. Soliton structures in $p(\phi)_2$. *Physical Review D*, American Physical Society (APS), v. 20, n. 12, p. 3120–3130, Dec. 1979. ISSN 0556-2821.

MANTON, N.; SUTCLIFFE, P. *Cambridge monographs on mathematical physics: Topological solitons*. Cambridge, England: Cambridge University Press, 2010.

MARJANEH, A. M.; SIMAS, F. C.; BAZEIA, D. Collisions of kinks in deformed φ^4 and φ^6 models. *Chaos, Solitons amp; Fractals*, Elsevier BV, v. 164, p. 112723, Nov. 2022. ISSN 0960-0779.

MUKHOPADHYAY, M.; SFAKIANAKIS, E. I.; VACHASPATI, T.; ZAHARIADE, G. Kink-antikink scattering in a quantum vacuum. *Journal of High Energy Physics*, Springer Science and Business Media LLC, v. 2022, n. 4, p. 118–147, Apr. 2022. ISSN 1029-8479.

MUNIYAPPAN, A.; RAVICHANDRAN, R.; MANIKANDAN, K. A bookshelf layer model for anti-kink and kink pair solitons in the ferroelectric liquid crystal. *Journal of Optics*, Springer Science and Business Media LLC, Dec. 2023. ISSN 0974-6900.

PAVA, J. A.; PLAZA, R. G. Unstable kink and anti-kink profile for the sine-gordon equation on a $\mathcal{Y}$-junction graph with $'$-interaction at the vertex. *Mathematische Zeitschrift*, Springer Science and Business Media LLC, v. 300, n. 3, p. 2885–2915, Nov. 2021. ISSN 1432-1823.

PESKIN, M.; SCHROEDER, D. *An introduction to quantum field theory*. London, England: CRC Press, 2019.

RAJANTIE, A. Magnetic monopoles in field theory and cosmology. *Philosophical Transactions of the Royal Society A: Mathematical, Physical and Engineering Sciences*, The Royal Society, v. 370, n. 1981, p. 5705–5717, Dec. 2012. ISSN 1471-2962.

RAJARAMAN, R. *Solitons and instantons. An introduction to solitons and instantons in quantum field theory*. Netherlands: Elsevier BV, 1982.

ROMANCZUKIEWICZ, T. Interaction between kink and radiation in ^{4} model. arXiv, 2003.

SANTOS, C. E. S.; CAMPOS, J. G. F.; MOHAMMADI, A. On the localized and delocalized modes in kink-antikink interactions: a toy model. 2024.

SUGIYAMA, T. Kink-antikink collisions in the two-dimensional 4 model. *Progress of Theoretical Physics*, Oxford University Press (OUP), v. 61, n. 5, p. 1550–1563, May 1979. ISSN 1347-4081.

SWIHART, J. C. Field solution for a thin-film superconducting strip transmission line. *Journal of Applied Physics*, AIP Publishing, v. 32, n. 3, p. 461–469, Mar. 1961. ISSN 1089-7550.

TONG, D. *Lectures on quantum field theory*. [S.l.: s.n.], 2006.

VACHASPATI, T. *Kinks and domain walls*. Cambridge, England: Cambridge University Press, 2006.

YAMALETDINOV, R. D.; SLIPKO, V. A.; PERSHIN, Y. V. Kinks and antikinks of buckled graphene: A testing ground for the φ^4 field model. *Physical Review B*, American Physical Society (APS), v. 96, n. 9, p. 094306, Sep. 2017. ISSN 2469-9969.

YANAGISAWA, T.; HASE, I. Massless modes and abelian gauge fields in multi-band superconductors. *Journal of the Physical Society of Japan*, Physical Society of Japan, v. 82, n. 12, p. 124704, Dec. 2013. ISSN 1347-4073.

YANAGISAWA, T.; HASE, I.; TANAKA, Y. Massless and quantized modes of kinks in the phase space of superconducting gaps. *Physics Letters A*, Elsevier BV, v. 382, n. 48, p. 3483–3489, Dec. 2018. ISSN 0375-9601.